3D bioengineered neural tissue generated from patient-derived iPSCs develops time-dependent phenotypes and transcriptional features of Alzheimer's disease

Selene Lomoio[1], Ravi S. Pandey[2], Nicolas Rouleau[3], Beatrice Menicacci[1], WonHee Kim[1], William L. Cantley[3], Philip G. Haydon[1], David A. Bennett[4], Tracy L. Young-Pearse[5], Gregory W. Carter[2,6], David L. Kaplan[3], and Giuseppina Tesco[1#]

[#] Corresponding author

Affiliations

[1] Department of Neuroscience, Tufts University School of Medicine, Boston, MA, USA

[2] The Jackson Laboratory for Genomic Medicine, Farmington, CT, USA

[3] Department of Biomedical Engineering, Tufts University, Medford, MA, USA

[4] Rush Alzheimer's Disease Center, Rush University Medical Center, Chicago, IL, USA

[5] Ann Romney Center for Neurologic Diseases, Brigham and Women's Hospital and Harvard Medical School, Boston, MA, USA

[6] The Jackson Laboratory, Bar Harbor, ME, USA

Email addresses

Selene Lomoio: selene.lomoio@tufts.edu

Ravi S. Pandey: ravi.pandey@jax.org

Nicolas Rouleau: nicolas.rouleau@algomau.ca

Beatrice Menicacci: beatrice.menicacci@tufts.edu

WonHee Kim: wonhee.kim@tufts.edu

William L. Cantley: william.cantley@gmail.com

Philip G. Haydon: philip.haydon@tufts.edu

David A. Bennett: david_a_bennett@rush.edu

Tracy L. Young-Pearse: tyoung@rics.bwh.harvard.edu

Gregory W. Carter: gregory.carter@jax.org

David L. Kaplan: david.kaplan@tufts.edu

Giuseppina Tesco: giuseppina.tesco@tufts.edu

53 **Abstract**

54 **Background**

55 Current models to study Alzheimer's disease (AD) include cell cultures and animal models.
56 Human diseases, however, are often poorly reproduced in animal models. Developing techniques
57 to differentiate human brain cells from induced pluripotent stem cells (iPSCs) provides a novel
58 approach to studying AD. Three-dimensional (3D) cultures to model AD are represented by
59 organoids, neurospheroids, and scaffold-based cultures. Some AD-related phenotypes have
60 been identified across 3D models [1]. However, to our knowledge, none of these studies could
61 recapitulate several AD-related hallmarks in one single model and establish a temporal relation
62 among them. Furthermore, to date, the transcriptomic features of these 3D models have not been
63 compared with those of human AD brains. These data are, in our opinion, key to understanding
64 the pertinency of these models for studying AD-related pathomechanisms over time.

65 **Methods**

66 We developed a 3D bioengineered model of iPSC-derived neural tissue that combines a porous
67 scaffold composed of silk fibroin protein with an intercalated collagen hydrogel to support the
68 growth of neurons and glial cells into complex and functional networks. This biomaterial scaffold,
69 designed to match the mechanical properties of brain tissue, can support 3D neural cultures for
70 an extended time without necrosis, a fundamental requisite for aging studies.

71 We have optimized our protocol by seeding neural precursor cells (NPCs) into these scaffolds.
72 NPC-derived cultures were generated from iPSC lines obtained from two subjects carrying the
73 familial AD (FAD) APP London mutation, two well-studied control lines, and an isogenic control.
74 Cultures were analyzed at 2 and 4.5 months.

75 **Results**

76 An elevated Aβ42/40 ratio was detected in conditioned media from FAD cultures at both time
77 points, as previously reported in 2D cultures derived from the same FAD lines. However,
78 extracellular Aβ42 deposition and enhanced neuronal excitability were observed in FAD culture

only at 4.5 months. The increased excitability of FAD cultures correlated with extracellular Aβ42 deposition but not with soluble Aβ42/40 ratio levels, as they were similar at both time points. These data suggest that extracellular Aβ deposition may trigger enhanced network activity. Notably, neuronal hyperexcitability has been described in AD patients early in the disease. Transcriptomic analysis revealed the deregulation of multiple gene sets in FAD samples. Notably, such alterations were similar to those observed in human AD brains in a large study that performed a co-expression meta-analysis of harmonized data from Accelerating Medicines Partnership for Alzheimer's Disease (AMP-AD) across three independent cohorts.

Conclusions

Our 3D tissue model supports the differentiation of healthy iPSC-derived cultures in a porous silk-collagen composite sponge with an optically clear central region. This design facilitates nutrient delivery to meet the metabolic demand of long-term cultures. These data provide evidence that our bioengineered model from patient-derived FAD iPSCs develops time-dependent AD-related phenotypes and establishes a temporal relation among them. Furthermore, FAD iPSC-derived neuronal tissue recapitulates transcriptomic features of AD patients. Thus, our bioengineered neural tissue represents a unique tool to model AD-related pathomechanisms over time, with several advantages compared to the existing models.

Keywords

Alzheimer's disease

Human iPSC

iPSC-derived cultures

Human neural cells

Bioengineered model

3D model

Background

Alzheimer's disease (AD) is a progressive neurodegenerative disorder characterized by memory impairments and cognitive deterioration. It is one of the most common forms of neurodegeneration and accounts for approximately 70% of all cases of dementia. The key pathological hallmarks of AD are extracellular senile plaques composed of neurotoxic amyloid-beta (Aβ) peptide and intracellular neurofibrillary tangles (NFT) composed of hyperphosphorylated tau [2]. Clinical studies show that the most critical risk factors for AD are aging and family history of the disease. Approximately 5% of the population over 65 is affected by AD, and its prevalence doubles with every five years of increasing age [3]. Less than 1% of AD cases occur in families where the disease is inherited in a fully penetrant, autosomal dominant manner, with early (< 65) onset. Three early-onset familial AD (FAD) genes have been identified to date: the amyloid precursor protein (APP) gene, the presenilin 1 (PSEN1) gene, and the presenilin 2 (PSEN2) gene. Together, these genes can harbor any of > 400 mutations (https://www.alzforum.org/mutations) that account for roughly 5-10% of autosomal dominant FAD.

Current models to study AD include cell cultures and animal models. Human diseases, however, are often poorly reproduced in animal models [4]. A significant limitation of using rodents to model AD is the increasing evidence for marked differences between humans and rodents in glial gene expression, in contrast to the relatively conserved neuronal gene expression across mammals [5-7]. The development in the past decade of techniques to generate human-induced pluripotent stem cells (iPSCs) and differentiate them into different brain cell types, together with advances in genome editing, has provided a novel model to study AD and other neurodegenerative disorders [1, 8]. Neural cultures derived from patients or isogenic mutant iPSCs recapitulate at least some of the phenotypes observed in the AD brain [1, 8, 9]. However, conventional two-dimensional (2D) culture systems fail to recapitulate the diversity and maturation of multiple cell types and their interaction under physiological and pathological conditions. For example, removing secreted Aβ

129 with media changes most likely prevents the deposition of amyloid aggregates in 2D cultures [1].
130 To date, three-dimensional (3D) cultures to model AD are represented by organoids,
131 neurospheroids, and scaffold-based 3D cultures (for review, see [1]). Some AD-related
132 phenotypes have been identified across 3D models [1]. However, to our knowledge, none of these
133 studies could recapitulate several AD-related hallmarks in one single model and establish a
134 temporal relation among them. Furthermore, to date, no studies have compared the
135 transcriptomic features of human 3D models to those of human AD brains. These data are, in our
136 opinion, key to understanding the pertinency of these models for studying AD-related
137 pathomechanisms over time.
138 We developed a bioengineered model of iPSC-derived neural tissue [10]. This biomaterial scaffold
139 design was adapted from our previous tissue model generated using primary embryonic rodent
140 brain cells [11] and human-induced neural stem cells [12, 13] to match the mechanical properties
141 of native brain tissue. Our silk-collagen-based "donut" scaffolds can support compartmentalized,
142 3D neural-like tissues for over a year without necrosis [14]. More importantly, our cultures develop
143 networks and action potentials (APs) typical of fully mature neurons [10]. The architecture of the
144 scaffolds was optimized to meet the metabolic demand of high-density cultures in terms of free
145 diffusion of nutrients and oxygen, a fundamental requisite for long-term cultures and aging-related
146 studies.
147 To support that our bioengineered tissue model can reproduce AD-related phenotypes, we have
148 generated cultures from iPSC lines obtained from two subjects carrying the FAD mutation APP
149 V717I (also known as London), hFAD-1, and hFAD-2 (Clone A and B) [15]. As controls, we used
150 two well-studied lines, YZ1 and BR24 [9, 15]. Furthermore, we generated the isogenic control of
151 the hFAD-2 Clone B line by correcting the APP V717I mutation to wild type (C-hFAD-2 Clone B).
152 FAD and control cultures were analyzed at two time points (2 and 4.5 months). An elevated
153 Aβ42/40 ratio was detected in FAD cultures at both time points, as previously reported in 2D
154 cultures derived from the same FAD lines [15].

155 Additionally, extracellular Aβ42 deposition and enhanced neuronal excitability were observed in
156 FAD culture at 4.5 months. Remarkably, neuronal hyperexcitability has been described in both
157 FAD and late-onset AD (LOAD) patients at the early stage of the disease [16]. Gene expression
158 analysis was performed to identify the specific target genes which exhibit significantly increased
159 or decreased expression in FAD lines compared to controls at both time points. Multiple gene
160 sets were deregulated in FAD samples at 2 months. The difference was maintained up to 4.5
161 months. Several of the pathways identified are implicated in neurotransmitter release/reuptake
162 and synthesis/storage, neural connectivity, structural stability of the cytoskeleton, axonal and
163 dendrite structure, and vesicle trafficking regulation. Such alterations in gene expression were
164 similar to those observed in human AD brains in a large study that performed a co-expression
165 meta-analysis of harmonized Accelerating Medicines Partnership for Alzheimer's Disease (AMP-
166 AD) data across three independent cohorts [17]. These data provide compelling evidence that our
167 3D cultures reproduce some time-dependent phenotypes and transcriptomic features observed
168 in AD patients. Thus, our bioengineered neural tissue represents a valuable model for studying
169 AD-related pathomechanisms over time.
170

171 **Results**

172 **A 3D bioengineered silk-collagen neural model**

173 We have previously designed and validated a 3D bioengineered neural model that combines a
174 porous scaffold composed of silk fibroin with an intercalated hydrogel to allow neurons and glial
175 cells to grow into complex and functional networks [11, 13, 18]. Each element of this model was
176 designed to be tunable, from the pore sizes in the scaffold biomaterial [19] to the hydrogel
177 composition, mechanical properties, and incorporated cell types [14]. We demonstrated that
178 iPSCs incorporated into the scaffolds could directly differentiate into neurons and glial cells and
179 remain functionally active for several months [10].

180 We have optimized our protocol for this study by seeding neural precursor cells (NPCs) instead
181 of iPSCs. This improved protocol offers several advantages: NPCs can be expanded, frozen,
182 banked, and subsequently differentiated. Having NPC stocks derived from multiple subjects
183 allows synchronization of their differentiation and minimizes experimental variability. We have
184 successfully generated NPCs from various iPSC lines using an embryoid body (EB)-based
185 protocol [15, 20-22] that seeks to recapitulate embryonic differentiation. In the absence of
186 exogenous patterning factors, the default path of this protocol is to generate forebrain neurons of
187 cortical fates [23].
188 For the success of this experimental strategy, quality control parameters are associated with iPSC
189 cultures [24]. iPSCs are susceptible to cell culture stresses and prone to genomic instability.
190 Morphology is an obvious indicator of the iPSC health [24]. In our practice, karyotyping, potency,
191 and mycoplasma testing have been routinely performed in all iPSC lines used for this study (Fig.
192 1A-B, Fig. S1).
193 Figure 1C illustrates the timeline schematic for the protocol, in which well-defined and compact
194 iPSC colonies expressing pluripotency markers like the octamer-binding transcription factor 4
195 (Oct4) are differentiated to NPCs over approximately 20 days. The milestones of this approach
196 are the formation of EBs, three-dimensional cell aggregates that mimic some structures of the
197 developing embryo. They can differentiate into all three germ layers [25], followed by neural
198 rosette maturation that can be identified morphologically by their characteristic appearance as
199 round clusters of primitive neuroepithelial cells with apicobasal polarity [26] (Fig. 1C).
200 According to previous work, nestin-positive NPCs can be robustly passaged, frozen, thawed, and
201 differentiated into functional neurons. NPCs could be typically passaged more than ten times in
202 vitro without accumulating karyotype abnormalities [26]; however, in agreement with other studies
203 [26, 27], we found that beyond ten passages, NPCs show increased cellular heterogeneity and
204 lower differentiation efficiency. Thus, experiments were conducted on mycoplasma-free passage-
205 matched NPC populations between passages two and six.

206 When differentiated in 2D on a poly-ornithine/laminin substrate using BrainPhys media
207 supplemented with SM1 and N2, NPCs can efficiently differentiate into human neurons
208 (hNeurons) expressing characteristic markers of a mature neuronal population such as the
209 microtubule-associated protein 2B (MAP2B), the neuron-specific class III beta-tubulin (Tuj1), and
210 synaptophysin (SYN) for extended periods. Glial fibrillary acidic protein (GFAP)-positive cells are
211 also observed, indicating the presence of astrocytic-like cells (Fig. 1D). NPCs have already been
212 described as having dual lineage potential and can differentiate into 70-80% neural populations
213 of Tuj1-positive neurons and 20-30% GFAP-positive astrocytes [26].
214 For this study, NPCs have been seeded into silk scaffolds and cultured according to the timeline
215 in Fig. 1E. Our data indicate that NPCs integrate into the silk-collagen scaffold model, expand
216 (NeuroFluor NeuO live staining, Fig. 1E), and differentiate into healthy neurons and astrocytic-
217 like cells, as indicated by IF imaging (Fig. 1F). Cultures express neuronal markers such as
218 neurofilament heavy chain (NFH), MAP2B, and Tuj1 together with GFAP (Fig. 1F). They develop
219 an intricated three-dimensional network extending deep into the silk pores and the supporting
220 collagen, suggesting high connectivity among growing cells (Fig. 1E, F). Cultures generated with
221 this approach supported by BrainPhys media supplemented with SM1 and N2 can survive in
222 culture for extended periods.
223
224 **Aβ42/40 ratio and extracellular Aβ42 deposition are elevated in FAD cultures**
225 To explore whether our bioengineered cultures could be valuable for modeling AD, we generated
226 cultures from extensively characterized iPSC lines [15] from a father (hFAD-1) and a daughter
227 (hFAD-2), each harboring the FAD mutation APP V717I [15] (Fig. 2A). The father was 57 years
228 old and diagnosed with AD before the biopsy. In contrast, the daughter was asymptomatic at age
229 33. The two clones from the daughter (hFAD-2 Clone A and Clone B) displayed a normal euploid
230 karyotype (Fig. S1), while the clone from the father (hFAD-1) revealed a standard chromosome
231 number but a balanced (t(1;12)(q42.3;q21.2)) translocation in all cells analyzed (Fig. S1). The

232 fibroblasts obtained from this subject displayed the same abnormal karyotype, suggesting a
233 preexisting abnormality that did not arise during the reprogramming [15]. This karyotypic alteration
234 didn't compromise the differentiation potential for the line.
235 The following lines were selected as controls (Fig. 2A). YZ1 [15], derived from fetal lung
236 fibroblasts, BR24 (Religious Order Study (ROS) or Rush Memory and Aging Project (MAP) [28]),
237 a cognitively unimpaired woman at the time of biopsy, 76 years of age [9]. Participants in the ROS
238 and MAP projects range from 50 to over 100 years and are free of dementia at the enrollment [9,
239 28]. Follow-up assessments indicated that the BR24 subject died at the age of 90, showing no
240 signs of cognitive decline or AD pathology. We also generated an isogenic control for the hFAD-
241 2 Clone B line (Fig. 2B) using genome-editing technology by reverting the APP V717I mutation to
242 wild type (C-hFAD-2 Clone B). Potential off-target cuts were identified using the Cas-OFF finder
243 (http://www.rgenome.net/cas-offinder). The top 8 sites were amplified, and Sanger sequenced to
244 verify the status of these potential off-targets. None of the predicted sites showed evidence of off-
245 targeting cutting. No karyotype clonal abnormalities were identified among the control lines (Fig.
246 S1).
247 To better understand the nature of our cultures and the reproducibility of the differentiation
248 approach from different iPSC lines and clones, we next turned to NanoString Technologies® for
249 measuring gene expression at 2 and 4.5 months. Data were analyzed by ROSALIND®
250 (https://rosalind.onramp.bio), with a HyperScale architecture developed by ROSALIND®, Inc.
251 (San Diego, CA, USA), and the nCounter® Advanced Analysis protocol. Housekeeping probes (9)
252 used for normalization were selected based on the geNorm algorithm implemented in the
253 NormqPCR R library.
254 We used the nCounter® Cell Type Profiling Module (as described in [29]) to assess the abundance
255 of various cell populations (Fig. 2C). The method quantifies cell populations using marker genes
256 expressed stably and precisely in given cell types. While markers for endothelial cells,
257 oligodendrocytes, astrocytes, neurons, and microglia have been screened, only scores for

258 neurons and astrocytes reached a statistically significant threshold (p-value <0.001 and <0.01,
259 respectively, Fig. 2C), indicating that these two cell types are the main constituents of our cultures.
260 Exploiting NanoString normalized expression analysis, we compared the expression of specific
261 groups of commonly expressed genes in iPSC-derived neural cultures (Fig. S2) based on
262 previous studies [15, 20, 23, 30-32] between different lines, genotypes, time points, and biological
263 replicates. In agreement with previous observations [15, 20], normalized expression analysis
264 identified the enrichment of a vast array of glial (GFAP, ALDH1L1, S100B, etc.), pan-neuronal
265 and synaptic markers (HOMER1, TBR1, STX1A, etc.) with most neurons exhibiting an excitatory
266 profile, together with some progenitor markers (NES, CCND1) being expressed up to 4.5 months
267 post-seeding. As expected, based on the differentiation method implemented, genomic analysis
268 suggests that our culture acquired a cortical layer fate as indicated by the expression of genes
269 (TBR1, DLX1, DLX2, etc.) involved in mammalian neocortical development and/or expressed in
270 a layer-specific manner in the human neocortex (Fig. S2) [33]. Also, AD-related genes were
271 expressed in our 3D cultures across all analyzed conditions. Differential expression analysis did
272 not reveal any significant variance between lines and genotypes for this set of genes, suggesting
273 that the cultures are homogeneously patterned, and that the differentiation approach is highly
274 reproducible.
275 To assess whether our cultures can recapitulate some AD-related phenotypes, soluble Aβ
276 quantification (MSD: Meso Scale Discovery Assay, Aβ Peptide Panel 1-4G8) was performed on
277 24-hour-conditioned media (Fig. 2D). In agreement with previous reports [15, 23, 34, 35], the
278 Aβ42 over Aβ40 ratio was found to be increased in FAD cultures compared to control ones at
279 both time points (CTR 2mo: 0.040±0.002 vs. FAD 2mo: 0.089±0.017, p=0.0003; CTR 4.5mo:
280 0.048±0.004 vs. FAD 4.5mo: 0.093±0.005, p<0.0001). The Aβ42/40 ratio calculated for the
281 isogenic C-hFAD-2 Clone B control was comparable to that of other control lines, supporting the
282 idea that the observed increase in the hFAD-2 Clone B depended on the APP V717I mutation.

283 Next, we performed IF using an antibody specific for Aβ42 (validated in 5XFAD:BACE1$^{-/-}$ brain
284 sections [36]) and calculated the amyloid burden for CTR and FAD cultures at both time points
285 (Fig. 2E). Confocal imaging and 3D reconstruction revealed the presence of Aβ42-positive
286 extracellular aggregates interspersed among FAD hNeurons (identified by MAP2B staining, Fig.
287 2F). Volumetric analysis of the amyloid burden (Fig. 2E) revealed a mild trend for increase starting
288 at 2 months in FAD cultures compared to controls (CTR: 0.00053±0.00022 vs. FAD:
289 0.00170±0.00044, p=0.9368) with a striking difference among conditions at 4.5 months (CTR:
290 0.00028±0.00005 vs. FAD: 0.02572±0.00281, p<0.0001). No difference was identified between
291 control groups at the two time points analyzed.
292
293 **FAD cultures manifest enhanced neuronal excitability**
294 To determine the electrophysiological properties of the cultures, local field potentials (LFPs) were
295 recorded from single electrodes inserted into the superficial layers of the hydrogel next to silk
296 fibers, adapting a protocol by Du and collaborators [37], where both spontaneous and evoked
297 potentials (EPs) were collected. LFPs, indicative of cellular electrical activations [14], were
298 quantified and compared across all conditions. The spontaneous and evoked activity was
299 observed within all the scaffolds analyzed starting at 2 months, suggesting that our 3D model is
300 populated by functional neurons capable of network activity.
301 Evidence indicates that LOAD and FAD patients show enhanced excitability, with onset during
302 the early stages of the pathology [38-45]. In our study, FAD cultures displayed comparable levels
303 of spontaneous potentials (Log10 LFP spikes/min) relative to control samples at 2 months (CTR:
304 0.717±0.130 vs. FAD: 0.872±0.126, p=0.3950); however, by 4.5 months, FAD samples displayed
305 significantly more spontaneous potentials relative to controls (CTR: 0.515±0.106 vs. FAD:
306 0.832±0.114, p=0.0475). Similarly, FAD samples showed more EPs relative to controls at 4.5
307 months post-seeding (CTR: 0.736±0.079 vs. FAD: 1.050±0.077, p=0.0064), which was not

308 apparent at 2 months (CTR: 1.040±0.091 vs. FAD: 1.270±0.112, p=0.1069). Our findings agree
309 with previous work that indicates dysregulation of the electrophysiological properties in AD brains
310 accompanied by enhanced network activity. Cognitive impairment in AD patients was assumed
311 to originate from depressed synaptic activity that eventually led to neurodegeneration. However,
312 multiple lines of evidence now indicate that, particularly during AD initial stages, synapse
313 dysfunctions are first induced by neuronal hyperactivity rather than hypoactivity [46-48].
314

315 **Differential expression and functional analysis of the NanoString panel in FAD cultures**

316 Transcriptional profiling of NanoString data from our samples was performed by ROSALIND®
317 platform (see method section for details). At 2 months, there were 133 differentially expressed
318 genes (DEGs) (absolute fold change > 1.5 & FDR < 0.05) between FAD and control samples (Fig.
319 4A). Expression for 38 of those 133 genes was upregulated in FAD samples compared to controls
320 and downregulated for 95 of 133 genes (Fig. 4A). Gene set analysis (GSA) identified increased
321 expression of genes associated with Cytokines, Activated Microglia, and Neuronal Cytoskeleton
322 (directed GSS > 0) (Fig. 4C).
323 Based on the differentiation protocol used for this study, we expected our cultures to be populated
324 exclusively by cells derived from the neuroectodermal lineage. So, we were surprised to observe
325 an upregulation of the Activated Microglia pathway in FAD cultures. Follow-up
326 immunofluorescence for TMEM119 (Fig. S3), a well-known microglia marker, followed by confocal
327 microscopy identified the presence of TMEM119 positive cells in the scaffolds interspersed
328 among MAP2 and GFAP-positive cells, indicating the presence of microglia-like cells in our
329 cultures. The cells show a ramified morphology and are intertwined with neuronal processes as
330 described by others (Fig. S3) [49]. These data agree with previous studies that have identified
331 mesoderm-derived progenitors and microglia in cerebral organoids [49, 50].

332 Further, GSA identified reduced expression of genes associated with multiple other
333 neurodegeneration pathways such as Transmitter Release, Neural Connectivity, and Vesicle
334 Trafficking (directed GSS < 0) (Fig. 4C).
335 At 4.5 months, there were 38 DEGs (absolute fold change > 1.5 & $p < 0.05$) between FAD and
336 control samples (Fig. 4B). Expression for 5 of the 38 genes was upregulated in FAD samples
337 compared to controls and downregulated for 33 of 38 genes (Fig. 4B). Gene set analysis identified
338 increased expression of genes associated with Cytokines and reduced expression of genes
339 associated with multiple pathways such as Transmitter Release, Neuronal Cytoskeleton, and
340 Vesicle Trafficking (Fig. 4D).
341
342 **FAD cultures reproduce human neurodegeneration signatures**
343 To assess the relevance of our model for AD, we performed a correlation analysis between our
344 NanoString data from FAD cultures and human post-mortem co-expression modules [17, 51].
345 FAD cultures at 2 months showed significant positive correlations ($p<0.05$) with AD-associated
346 changes in human co-expression modules in Consensus Cluster B, which include transcripts that
347 are enriched for immune-related pathways in the cerebellum brain region (CBEturquoise) (Fig.
348 5A). Furthermore, FAD cultures at 2 months showed significant positive correlations ($p<0.05$) with
349 AD changes in multiple modules in Consensus Cluster C, which include transcripts that are
350 enriched for neuronal-related pathways in the inferior frontal gyrus module (IFG), temporal cortex
351 (TCX), and the parahippocampus gyrus (PHG) brain regions (Fig. 5A). However, these significant
352 positive correlations diminish at 4.5 months (Fig. 5A). Interestingly, FAD cultures at 2 months
353 showed a significant positive correlation (Pearson Correlation = 0.27; $p<0.05$) with AD ECM
354 organization changes in module TCXblue in Consensus Cluster A but also showed a significant
355 negative correlation (Pearson Correlation = -0.35; $p<0.05$) with AD changes in the PHGyellow
356 module enriched for similar biological process. However, at 4.5 months of age, FAD cultures
357 exhibited a non-significant but positive correlation with AD changes in the PHGyellow module

358 (Pearson Correlation = 0.11; $p > 0.05$) and a stronger significant positive correlation with TCXblue
359 module changes in AD (Pearson Correlation = 0.27; $p < 0.05$) (Fig. 5A). These results suggest
360 that functional changes such as ECM organizations are strengthened with age and represent
361 similar effects to those observed in endpoint AD.
362 Next, we examined the expression profile of differentially regulated genes in the FAD cultures
363 identified by the ROSALIND® platform across human AMP-AD transcriptomic data. We
364 determined that most of the differentially upregulated genes (fold change > 1.5) in 2-month-old
365 FAD cultures showed increased expression in immune/inflammation-associated AMP-AD
366 modules in Consensus Cluster B (Fig. 5B), suggesting increased expression of these genes in
367 multiple human brain regions. Similarly, most of the differentially downregulated genes (fold
368 change < 1.5) in 2 months old FAD cultures showed reduced expression across numerous human
369 brain regions except in the frontal pole and cerebellum brain regions of AD patients (Fig. 5C). Our
370 2-month-old FAD cultures exhibited expression profiles of neuronal genes remarkably similar to
371 human AD for multiple brain regions.
372 Similarly, we examined the expression of differentially deregulated genes in 4.5 months old FAD
373 cultures across AMP-AD modules. There were only 5 genes that were differentially upregulated
374 in the 4.5-month-old FAD cultures compared to controls, and these genes mainly exhibited
375 reduced expression in some of the AMP-AD modules (Fig. S4 A). Most of the differentially
376 downregulated genes (fold change < 1.5) in 4.5 months old FAD cultures showed reduced
377 expression in neuronal-associated AMP-AD modules in Consensus Cluster C, except in
378 CBEyellow and FPyellow modules (Fig. S4 B). These results suggest that neurodegeneration-
379 related genes were downregulated in our FAD cultures, similar to human AD patients.
380

381 **Discussion**

382 We report here that iPSC-derived NPCs reliably integrate into the silk-collagen scaffold model,
383 expand, and differentiate in healthy neurons and astrocytic-like cells as indicated by the

384 expression of neuronal and astrocytic markers. Accordingly, gene expression and cell enrichment
385 analysis revealed a similar cellular composition across all cultures. More importantly, 3D neural
386 cultures from APP London mutation heterozygous carriers recapitulate some AD-like phenotypes.
387 We found that FAD cultures displayed an elevated Aβ42/40 ratio in conditioned media at 2 and
388 4.5 months, as previously reported in 2D cultures derived from the same FAD lines [15, 23]. While
389 the Aβ42/40 ratio change was similar at the two time points, extracellular deposition of Aβ42
390 developed only in the older cultures and identified FAD from control cultures. Notably, Aβ42/40
391 ratio and Aβ42 extracellular deposition in the isogenic control cultures were similar to BR24 and
392 YZ1 lines. These data demonstrate that the APP V7171I mutation causes such phenotypes.
393 LFP recordings showed that our 3D cultures were electrically active starting at 2 months. While
394 no difference in LFP frequency was observed at 2 months, by 4.5 months, FAD samples displayed
395 significantly higher spontaneous and evoked potentials relative to controls. The increased
396 excitability in FAD cultures correlated with extracellular Aβ42 deposition but not with soluble
397 Aβ42/40 ratio levels, as they were similar at both time points. These data suggest that extracellular
398 Aβ deposition may trigger enhanced network activity. Our data agree with previous work showing
399 increased neuronal excitability in AD patients at an early stage of the disease [16, 43].
400 A large study conducted on carriers of FAD mutations (The Dominantly Inherited Alzheimer
401 Network (DIAN) consortium) showed that changes in cerebrospinal fluid (CSF) biomarkers,
402 cerebral amyloid deposition, and brain metabolism begin at least two decades before the
403 predicted onset of clinical symptom [52]. Similarly, increased brain activity may precede AD
404 diagnosis by 30 years in PSEN1 mutation carriers [53, 54]. More recently, neuronal
405 hyperexcitability was described in organoids generated from isogenic iPSC lines carrying the FAD
406 PSEN1 ΔE9, PSEN1 M146V, or APP Swedish mutations [55]. However, this is the first report of
407 enhanced excitability in 3D cultures from patient-derived iPSC lines carrying the APP London
408 mutation.

409 Differential expression analysis and GSA revealed that multiple gene sets were deregulated in
410 FAD compared to control cultures. At 2 months, upregulated genes were associated with
411 Cytokines, Activated Microglia, and Neuronal Cytoskeleton pathways in GSA. The downregulated
412 genes were related to multiple neurodegeneration pathways such as Transmitter Release, Neural
413 Connectivity, and Vesicle Trafficking. Some of the differences were maintained for up to 4.5
414 months. At 4.5 months, GSA identified increased expression of genes associated with Cytokines
415 and reduced expression of genes associated with multiple pathways such as Transmitter
416 Release, Neuronal Cytoskeleton, and Vesicle Trafficking. While most DEGs in the FAD cultures
417 are expressed in neurons, genes associated with activated microglia were upregulated in FAD
418 cultures at 2 months. Even though only scores for neuronal and astrocyte markers reached a
419 statistically significant threshold in the nCounter® Cell Type Profiling Module, TMEM119-positive
420 cells are present in our cultures. Similarly, mesoderm-derived progenitors, from which microglia
421 originate, and mature microglia-like cells innately develop in cerebral organoids [49, 50].
422 To validate our cultures as an AD model in vitro, we applied a system biology approach developed
423 to evaluate AD mouse models [51]. A correlation analysis was performed between gene
424 expression changes in FAD cultures and changes in human AD cases in post-mortem co-
425 expression modules. We used a recent human molecular disease catalog based on harmonized
426 co-expression data from three independent postmortem brain cohorts (ROSMAP, Mayo, Mount
427 Sinai Brain bank) [56-58] and seven brain regions that define 30 human co-expression modules
428 and five consensus clusters derived from the overlap of those modules [17]. FAD cultures at 2
429 months showed significant positive correlations with human co-expression modules in Consensus
430 Cluster B, including transcripts enriched for immune-related pathways. They showed significant
431 positive correlations with multiple modules in Consensus Cluster C, including transcripts enriched
432 for neuronal-related pathways. However, these significant positive correlations diminish at 4.5
433 months of age.

434 Next, we examined the expression profile of differentially regulated genes in the FAD cultures
435 identified by the ROSALIND® platform across human AMP-AD transcriptomic data. We
436 determined that most of the differentially upregulated genes in 2-months-old FAD cultures showed
437 increased expression in immune/inflammation-associated AMP-AD modules in Consensus
438 Cluster B. Similarly, most of the differentially downregulated genes in 2-months-old FAD cultures
439 showed reduced expression across numerous human brain regions in Consensus Cluster C.
440 Thus, 2-month-old FAD cultures exhibited expression profiles of neuronal genes remarkably
441 similar to human AD for multiple brain regions. In the 4.5-month-old FAD cultures, most
442 differentially downregulated genes showed reduced expression in neuronal-associated AMP-AD
443 modules in Consensus Cluster C. These results suggest that neurodegeneration-related genes
444 were downregulated in FAD cultures, similar to human AD patients.
445 Since iPSC reprogramming rejuvenates cells and erases donor aging signatures, concerns were
446 raised about the ability to model age-related diseases with iPSC-derived neuronal cultures [59].
447 It is well-established that AD develops over decades [60]. Thus, genetic factors may produce
448 endophenotypes early in life; therefore, they can be captured in iPSC-derived neural cultures.
449

450 **Conclusions**

451 We developed a neural tissue model that supports the differentiation of iPSC-derived NPCs in a
452 donut-shaped porous silk sponge with an optically clear (collagen-filled) central region. The
453 porous design facilitates nutrients and oxygen diffusion to meet the metabolic demand of long-
454 term cultures. This study provides compelling evidence that our 3D bioengineered model from
455 patient-derived FAD iPSCs develops time-dependent phenotypes and transcriptomic features
456 observed in AD patients. Some of these changes have been identified across other 3D models
457 [1]. However, to our knowledge, none of these studies could recapitulate several different AD-
458 related hallmarks in one single model. While Aβ extracellular deposition and changes in the
459 Aβ42/40 ratio represent frequent findings in other 3D models, the enhanced excitability and

460 transcriptomic changes described in our manuscript have been difficult to recapitulate in these
461 conditions. Importantly, in our scaffolds, these phenotypes have been identified at two time points
462 (2 and 4.5 months), resembling some of the features that characterize AD progression. Aβ42/40
463 ratio and transcriptomic changes are already present at 2 months, while Aβ deposition appears
464 only at 4.5 months when the neuronal hyperexcitability becomes evident, suggesting a temporal
465 relation between these two events. Gahtak et al. [55] detected hyperexcitability in AD organoids
466 accompanied by increased Aβ immunostaining and an increase in the ratio of secreted Aβ42/40
467 at 2 months; nevertheless, no other time points were analyzed, providing no information on the
468 temporal relation between these events. To date, no other studies have been published examining
469 the transcriptomic features of these 3D models while comparing them to those of human AD
470 brains in a large study that performed a co-expression meta-analysis of harmonized data from
471 Accelerating Medicines Partnership for Alzheimer's Disease (AMP-AD). These data are, in our
472 opinion, key to understanding the pertinency of these models for studying AD-related
473 pathomechanisms over time. As discussed, one of the main strengths of this model is that every
474 element was designed to be tunable and amenable to experimental modification. Although we did
475 not incorporate a layered structure for this study, the 3D model can be designed using a concentric
476 toroidal scaffold to more closely approximate gross features of the layered brain tissue [11].
477 However, we need to consider that any modification to the structural design of the model could
478 cause unexpected changes to the integrity and longevity of the cultures [14] and therefore require
479 extensive and costly troubleshooting. We could also incorporate embedded electrodes for
480 continuous, long-term recordings of electrophysiological activity [61, 62]. Moreover, unlike self-
481 organizing organoids, mixed 3D neuronal tissue could be generated by co-culturing neurons,
482 astrocytes, and microglia derived from different donors or isogenic iPSC lines carrying AD-linked
483 genetic variants [63]. For example mixed 3D cultures containing mutant neurons and wild-type
484 astrocytes or microglia cells and vice-versa could be used to study the impact of cell specific

genetic variants on AD-like phenotypes. For all these reasons, our bioengineered neural tissue represents a unique tool to model AD-related pathomechanisms over time, with several advantages and potential compared to the existing model.

On the other hand, our model still has technical limitations. Even though the porous structure of the scaffolds facilitates the diffusion of oxygen and nutrients, it lacks a proper neurovascular unit, a perivascular compartment, and coordinated drainage of accumulated metabolites. In addition, other practical challenges like scalability and high throughput screening compatibility will have to be optimized.

Methods

iPSC lines

hFAD-1, hFAD-2 Clone A and B iPSC lines [15] were generated in the laboratory of Dr. T. Young-Pearse (Brigham and Women's Hospital, Boston, MA, USA). BR24 iPSC line (ROSMAP) [9, 28] was generated at the New York Stem Cell Foundation. YZ1 iPSC line was obtained from the University of Connecticut-Wesleyan Stem Cell Core (Farmington, CT, USA [15]). The original manuscripts cited above describe the reprogramming methods and quality control assays for these lines.

hFAD-2 Clone B Corrected was generated at the University of Connecticut-Wesleyan Stem Cell Core (Farmington, CT, USA). Briefly, the guide RNA used for APP editing was designed using chop-chop (https://chopchop.cbu.uib.no/) for specificity to the loci of interest. The resulting guide 5' GACAGTGATCATCATCACCT 3' was identified to have high specificity to the desired loci. The guide is designed to cut the mutant allele. Given that the CAS9/guide RNA was transiently expressed in the cells, the potential for off-targets in the nearest matches was minimal. Potential off-targets were identified using the Cas-OFF finder (http://www.rgenome.net/cas-offinder/). The top eight identified sites were amplified from the clones, and Sanger sequenced to verify the status of these potential off-targets. None of the predicted sites showed evidence of off-targeting

511 cutting. After targeting, the corrected allele resulted in a single base difference from the original
512 guide sequence. None of the clones sequenced exhibited off-target cutting at the predicted sites
513 or the corrected allele.
514 All iPSC lines have been confirmed by sequencing before starting any of the experiments listed
515 in this manuscript.
516
517 **ROSMAP study participants**
518 iPSC lines were generated from autopsied participants in either the Religious Orders Study or
519 Rush Memory and Aging Project (ROSMAP) [28]. Both studies were approved by an Institutional
520 Review Board of Rush University Medical Center; they enroll older persons without dementia who
521 agree to annual clinical evaluation and brain donation at death. All participants signed informed
522 consent, an Anatomical Gift Act, and a repository consent to allow their resources to be
523 repurposed. As part of the annual evaluation, peripheral blood mononuclear cells were drawn and
524 cryopreserved.
525
526 **Karyotype analysis and mycoplasma testing**
527 G-banded karyotyping was outsourced to WiCell (Madison, WI, USA). WiCell's chromosome
528 analysis is optimized for pluripotent stem cells. All results are reviewed by an American Board of
529 Medical Genetics and Genomics (ABMGG) board-certified or board-eligible director. Karyograms
530 for all the lines have been checked every ten passages.
531 Mycoplasma testing was performed monthly for all the lines included in this study at any
532 differentiation stage (LookOut Mycoplasma PCR Detection Kit, Sigma). All cells used in this study
533 were consistently negative.
534
535
536

537 **NPC differentiation**

538 iPSCs were maintained in feeder-free conditions on plates coated with Matrigel hESC-qualified
539 Matrix (Corning) with daily media changes using mTeSR1 medium (StemCell Technologies).
540 Cells were held at 37°C and 5% CO_2 and were split as necessary based on colony growth (5-7
541 days). Cells were passaged in small aggregates (1:7/1:10 depending on the line) using ReLeSR
542 (StemCell Technologies). 10 µM Y-27632 (ROCK inhibitor, StemCell Technologies) were added
543 to the culturing media for a maximum of 24 hours after passage.

544 According to the StemCell Technologies method, NPCs were differentiated using an EB-based
545 protocol without SMADi supported by STEMdiff Neural Induction medium (StemCell
546 Technologies) with daily media change over ~20 days. To generate iPSC-derived EBs for neural
547 induction AggreWell 800 (StemCell Technologies), 24-well plates were used. These plates enable
548 the easy generation of uniformly sized EBs, making differentiation experiments more
549 reproducible. For each well of the AggreWell plate, $3x10^6$ single-cell suspension (Gentle Cell
550 Dissociation Reagent, StemCell Technologies) of iPSCs were plated, followed by centrifugation
551 at 100xg for 3 minutes, to capture the cells in the microwells. A daily partial-medium change was
552 performed for 4 days. On day 5, EBs were harvested from a single well of an AggreWell 24-well
553 plate and re-plated onto a Matrigel hESC-qualified-coated well of a tissue culture-treated 6-well
554 plate. Replated EBs were maintained with daily media change until neural rosette structures were
555 visible and defined. Around days 10-12, based on the different lines, rosettes were selected
556 (Neural Rosette Selection Reagent, StemCell Technologies) and replated onto Matrigel hESC-
557 qualified Matrix-coated plates. Selected rosette-containing clusters attach, and NPC outgrowths
558 will form a monolayer between the clusters. A daily full-medium change was performed. NPCs
559 are ready for passage 1 at approximately day 17-19 (Accutase, StemCell Technologies). NPCs
560 were plated at $1.25x10^5$ cells/cm^2 on Matrigel hESC-qualified Matrix-coated wells and maintained
561 in Neural Progenitor medium (StemCell Technologies) with daily complete media change. Single-
562 cell suspensions ($2x10^6$ cells/mL) of NPCs were cryopreserved and banked for future usage using

563 Neural Progenitor Freezing (StemCell Technologies). At least two separate differentiations of
564 NPCs have been generated from different iPSC stocks for all the lines included in this study and
565 used to differentiate hNeurons.
566
567 **Scaffold preparation, seeding, and differentiation into hNeurons**
568 Silk protein was processed from *Bombyx mori* cocoons as described previously [64]. In brief, silk
569 cocoons were cut into fragments and boiled for 30 minutes in a 0.02 M Na_2CO_3 solution. The
570 fibroin was solubilized in a 9.3 M LiBr solution dialyzed against deionized water. The silk solution
571 was then diluted to 6% weight/volume and used to generate the porous scaffolds via salt leaching
572 [19], using 500–600 um NaCl crystals to generate a sponge-like structure. A biopsy punch was
573 used to generate the donut-shaped scaffolds (5mm outer diam. x 2mm central hole diam. x 2mm
574 ht.). Scaffolds were autoclaved and then coated with poly-L-ornithine (20ug/mL in DPBS, Sigma)
575 and laminin (10ug/mL in DMEM/F-12, Sigma) overnight at 4°C.
576 A strained (40um nylon mesh) single-cell suspension of ($2x10^6$/100 uL) NPCs between passages
577 two and six was added to the coated scaffold in a 96-well plate and incubated for 24 hours. The
578 media (200uL, Neural Progenitor medium) was changed daily for five days following seeding,
579 moving the scaffolds to fresh wells with each change. After allowing five days of cellular
580 expansion, the scaffolds were moved to a clean well and infused with a 100 uL solution of cold
581 Collagen Type-1 Rat Tail (3.0mg/mL, Corning) mixed with 10X PBS and 1N NaOH (ratio 88:10:2).
582 The collagen-filled scaffolds were then incubated at 37°C until the gelation occurred (~45
583 minutes). Once solidified, the scaffolds were transferred to a 24-well plate and flooded with 1.5
584 mL of BrainPhys media (StemCell Technologies) supplemented with SM1 (StemCell
585 Technologies) and N2 (ThermoFisher) with media changes every four days and differentiated into
586 hNeurons.
587
588

589 **Immunofluorescence and imaging analysis**

590 2D and 3D cultures were fixed with a 4% paraformaldehyde/4% sucrose solution in DPBS for 15
591 and 30 minutes, respectively, followed by membrane permeabilization with 0.3% Triton X-100 for
592 15 minutes. Non-specific binding sites were blocked for one (2D) or four (3D) hours at RT (5%
593 BSA, 0.1% Triton-X-100 in DPBS). Cultures were then incubated with primary antibodies (see
594 Antibody Table) diluted in 1% BSA, 0.1% Triton-X-100 in DPBS overnight at 4°C. After multiple
595 washes in DPBS, sections were incubated with Alexa (1:1000 in 1% BSA in DPBS) fluorescent
596 secondary antibodies against the corresponding host species for one (2D) or three (3D) hours at
597 RT. Nuclei were stained with DAPI (Sigma). 2D cultures were mounted on superfrost slides
598 (Fisher Scientific) using Fluoromount-G1 mounting media (Southern Biotech), while 3D cultures
599 were imaged directly.

600 NeuroFluor™ NeuO (StemCell Technologies), a membrane-permeable fluorescent probe that
601 selectively labels iPSC-derived neurons, was used to stain live cultures according to manufacture
602 instructions.

603 Z-stack fluorescence images were obtained using confocal microscopes (SP8 Falcon Leica, SP8
604 Leica, see figure legends for details), keeping constant imaging parameters. 3D reconstructions
605 were generated with the LAS X Life Science Leica software. Image analysis was performed using
606 Fiji ImageJ version: 2.0.0-rc-69/1.52p.

607 Aβ burden volumetric analysis was performed using the Fiji ImageJ plug-in 3D object counter.
608 The sum of all extracellular Aβ deposition volumes was divided by the total volume of the region
609 of interest (ROI) imaged to obtain the amyloid burden values. At least two separate sets of cultures
610 per line and three images per set of cultures have been analyzed.

611

612 **MSD assay and data analysis**

613 Before harvest, BrainPhys media was changed, and fresh media was dispensed into each well.
614 Twenty-four hours later, media was collected and stored at -80°C. MSD (Rockville, MD, USA)

615 assay for the detection of human Aβ38, Aβ40, and Aβ42 (V-PLEX Aβ Peptide Panel 1 (4G8) Kit)
616 was performed in-house according to the manufacturer's instructions on undiluted conditioned
617 media. Technical duplicates were run for all the samples analyzed. The assay demonstrated high
618 sensitivity with a lower limit of detection values in the low-pg/mL and over 2.5 logs of dynamic
619 range, allowing the measurement of analytes in all samples, except for Aβ38, which fell under the
620 lower limit of detection for most of the samples. All MSD assays exhibited excellent reproducibility
621 with an average calculated concentration of 3.6% and 7.2% for the standards and samples within
622 the detection range of the assay, respectively. The data were analyzed using MSD Workbench
623 4.0 software. The software fits the standard curves using a four-parameter logistic fit with $1/y^2$
624 weighting.
625
626 **LFP recordings**
627 Local field potentials (LFPs) were recorded from samples, adapting a protocol by Du et al. [37].
628 Both spontaneous and evoked potentials (EPs) were collected. Each sample was placed in the
629 center of a 35mm plastic petri dish (Corning) containing 2 mL of an extracellular solution
630 simulating cerebrospinal fluid (mM): 130 NaCl, 1.25 NaH_2PO_4, 1.8 $MgSO_4$, 1.6 $CaCl_2$, 3 KCl, 10
631 HEPES-NaOH, 5.5 glucose, pH 7.4. The dish and solution were maintained at 37ºC using a WP-
632 16 Warmed Platform (with a TC-134A Handheld Temperature Controller). A bipolar stimulator
633 was positioned on top of the sample, affixing it to the bottom of the dish. Then, a recording
634 electrode (borosilicate glass pipette, 40-80 MΩ resistance) which was pulled with a Sutter P-97
635 (Navato), was inserted into the silk-scaffold region between the stimulators (e.g., stimulator-
636 electrode-stimulator). LFPs were amplified and digitized (Axon Instruments DAC; Intan digital
637 amplifier) with a sampling frequency of 2500Hz. Recordings were performed blind (each sample
638 was given an unidentifiable ID), always counterbalanced by condition, and replicated batches
639 were measured within the same 12-hour window.

640 Spontaneous activity (baseline) was recorded for 2 mins, followed by the evoked potential phase,
641 which consisted of a 60s period of stimulation (1ms pulse, 1Hz, 5 mA), an injection of 10 μM
642 tetrodotoxin (sodium channel blocker), 2 mins of perfusion, and a final 60 sec period of stimulation.
643 Data were retrieved from Clampex 10.7 (Axon Instruments), exported to Clampfit 10.7, and
644 "spikes" indicative of activity were extracted using an amplitude threshold (±0.35 mV). Spike
645 frequencies (LFP spikes/minute) were computed for spontaneous (baseline) recordings. Evoked
646 potentials per stimulation period were also quantified after a background-subtraction process as
647 previously described [37]. All data were normalized to DNA content quantified using Quant-iT
648 PicoGreen dsDNA Assay kit (ThermoFisher). Data were also subjected to a log-10 transformation
649 to stabilize and normalize expected trial-to-trial variation.
650
651 **RNA isolation and NanoString outsourcing**
652 At the time of desired analysis, scaffolds were snap-frozen using liquid nitrogen and stored at
653 −80°C. The frozen scaffolds were then homogenized using a liquid nitrogen-chilled Spectrum
654 Bessman Tissue Pulverizer (Fisher Scientific). RNA from homogenized samples was extracted
655 immediately after the homogenization using the RNeasy Plus Mini kit (Qiagen) following the
656 manufacturer's instructions. Briefly, samples were dissolved in Qiagen RLT Plus lysis buffer
657 supplemented with 1% β-mercaptoethanol and centrifuged for 3 min at maximum speed. The
658 supernatant was transferred to a gDNA Eliminator spin column to remove genomic DNA, and the
659 flow-through was mixed with 70% ethanol and placed in an RNeasy spin column. After one wash
660 with the RW1 buffer and two washes with the RPE buffer, RNA was eluted in 20uL of RNase-free
661 water and quantified using a NanoDrop 1000 Spectrophotometer (ThermoFisher). RNA
662 concentration was normalized to 20ng/uL, and 150ng of total RNA was shipped to NanoString
663 Technologies® (Seattle, WA, USA) for analysis.
664
665

666 **NanoString neuropathology panel gene expression profiling**

667 The NanoString Neuropathology profile panel was used for gene expression profiling of our RNA
668 samples on the nCounter platform (NanoString Technologies®, Seattle, WA, USA). The
669 neuropathology panel incorporated 770 human genes, including 10 references (housekeeping
670 genes) and 760 endogenous genes, to target all aspects of neurodegeneration. Data were
671 analyzed by ROSALIND® (https://rosalind.onramp.bio), with a Hyperscale architecture developed
672 by ROSALIND, Inc. (San Diego, CA, USA). Normalization, fold changes, and p-values were
673 calculated using criteria provided by NanoString. ROSALIND® follows the nCounter® Advanced
674 Analysis protocol of dividing counts within a lane by the geometric mean of the normalizer probes
675 from the same lane.

676 Housekeeping probes for normalization were selected based on the geNorm algorithm
677 implemented in the NormqPCR R library [65]. Fold changes, and significance score (p-value)
678 were calculated using the optimal method described in the nCounter® Advanced Analysis 2.0
679 User Manual. Significant p-values ($p < 0.05$) were adjusted for multiple genetic comparisons using
680 the Benjamini–Hochberg method of estimating false discovery rates [66]. Gene expression was
681 considered significantly different if there was a greater than 1.5. fold change compared to controls.
682 The nCounter Neuropathology profile panel annotation database was referenced to perform gene
683 set enrichment analysis. Directed global significance scores (GSS) were calculated relative to a
684 set of background genes measured in the experiment. This analysis determined both significance
685 and directional response (i.e., upregulated or downregulated) of GSS for a given
686 neurodegeneration pathway. A total of 24 fundamental neurodegeneration pathways were
687 examined to determine the effect of FAD mutation. Bar plots were generated to compare
688 neurodegeneration pathways as a function of directed GSS.

689

690

691

692 **AMP-AD post-mortem brain cohorts and gene co-expression modules**

693 Data on the 30 human AMP-AD co-expression modules were obtained from the Synapse data
694 repository [56, 58, 67] (https://www.synapse.org/#!Synapse:syn11932957/tables/;SynapseID:
695 syn11932957). These modules were obtained from a co-expression meta-analysis of harmonized
696 AMP-AD data across three independent study cohorts. Each module is enriched in genes
697 differentially expressed in AD cases versus controls [17]. The 30 AMP-AD modules were further
698 grouped into five consensus clusters that describe the major functional groups of alterations
699 observed in human AD [17, 51].

700

701 **iPSC-derived cultures-human brains expression comparison**

702 The nSolver software-generated raw gene expression counts for the Neuropathology panel.
703 Normalization was done by dividing counts within a lane by the geometric mean of the
704 housekeeping genes from the same lane. Next, normalized count values were log-transformed
705 for downstream analysis. To determine the effect of FAD mutation, we fitted a linear mixed-effect
706 regression model using the lme4 function in R by considering the fixed effect of FAD mutation
707 plus random variation in intercept among cell lines within controls and FAD mutation (formula ~
708 FAD + 1|FAD:Cell.Line).

709 To compare expression changes in FAD lines with those observed in human disease, we
710 computed Pearson correlations between log fold change in transcript expression of human AD
711 patients compared to control patients (Log2FC(AD/controls) and the effect of FAD mutation
712 estimated by the linear mixed-effect regression model [51, 68]. Correlation coefficients were
713 computed using the cor.test function built-in R as: cor.test(log2FC(AD/Control,β_{FAD}).

714 LogFC values for human transcripts after correction for technical covariates were obtained via the
715 AD Knowledge Portal (https://www.synapse.org/#!Synapse:syn14237651).

716

717

718 **Statistical analysis**

719 Information regarding statistical analyses can be found in the figure legends. Data are expressed
720 as the mean ± standard error of the mean (SEM), represented as error bars. All statistical tests
721 were computed using GraphPad Prism 9 software unless otherwise noted. ROUT method (1%)
722 was applied to identify outliers. A p-value of 0.05 was used as the significance threshold
723 throughout this study. In all figures, p-values are illustrated for all tests used: $^{n.s.}$ $p > 0.05$, * $p <$
724 0.05, ** $p \leq 0.01$, *** $p \leq 0.001$, **** $p \leq 0.0001$. A minimum of two differentiations for each iPSC
725 line have been analyzed for all experiments. Figure legends and graphs representing individual
726 data points indicate the sample size (n = number of scaffolds).

727

728 **List of supplementary materials:** Fig. S1, Fig. S2, Fig. S3, Fig. S4, Table 1.

729 **Availability of data and materials:** All data generated or analyzed during this study are included
730 in this published article and its supplementary information files. Additional information is available
731 from the corresponding author on request. ROSMAP resources can be requested at
732 https://www.radc.rush.edu.

733 **Competing interests:** SL, RSP, NR, BM, WK, WLC, PGH, DAB, TLYP, GWC, DLK, and GT have
734 no conflict of interest to declare.

735 **Funding:** This work was supported by awards from the National Institutes of Health:
736 1R21AG065792 (to GT), 5R01AG061838 (to GT, PGH, and DLK), R01AG055909 (to TLYP), and
737 U54AG054345 (to GWC). ROSMAP is supported by P30AG10161, P30AG72975, R01AG15819,
738 R01AG17917. U01AG46152, U01AG61356 (to DAB).

739 **Authors' contributions:** The authors confirm contributions to the manuscript as follows:
740 conceptualization: SL, GT; data curation: SL, RSP, NR; formal analysis: SL, RSP, NR;

investigation: SL, NR, BM, WK, WLC; methodology: SL, RSP, NR, GWC; resources: WLC, GWC, DAB, TLYP, DLK; project administration: GT; supervision: SL, GWC, DLK, GT; validation: SL, RSP, NR, BM, WK, GT; visualization: SL, RSP, NR; writing - original draft preparation: SL, RSP, NR, GT; writing - review and editing: SL, RSP, NR, BM, WK, WLC, PGH, DAB, TLYP, GWC, DLK, GT.

Acknowledgments: We thank Rachel Willen, Edward K. Robinson, Griffin Sigal, and Isabel Paine for their technical support.

Abbreviations:

2D: Two-Dimensional

3D: Three-Dimensional

Aβ: Amyloid Beta

AD: Alzheimer's Disease

AMP-AD: Accelerating Medicines Partnership for Alzheimer's Disease

AP: Action Potential

APP: Amyloid Precursor Protein

CBE: Cerebellum

CSF: Cerebrospinal Fluid

DEG: Differentially Expressed Gene

DIAN: Dominantly Inherited Alzheimer's Network

EB: Embryoid Body

EP: Evoked Potential

FAD: Familial Alzheimer's Disease

GFAP: Glial Fibrillary Acidic Protein

GSA: Gene Set Analysis

766 hNeuron: Human Neuron

767 IFG: Inferior Frontal Gyrus

768 iPSC: Induced Pluripotent Stem Cell

769 LOAD: Late-Onset Alzheimer's Disease

770 LFP: Local Field Potential

771 MAP2B: Microtubule-Associated Protein 2B

772 MSD: Meso Scale Discovery

773 NFH: Neurofilament Heavy Chain

774 NFT: Neurofibrillary Tangles

775 NPC: Neural Precursor Cell

776 Oct4: Octamer-Binding Transcription Factor 4

777 PHG: Parahippocampus Gyrus

778 PSEN1: Presenilin 1

779 PSEN2: Presenilin 2

780 ROSMAP: Religious Order Study Rush Memory and Aging Project

781 SYN: Synaptophysin

782 TCX: Temporal Cortex

783 Tuj1: Neuron-Specific Class III Beta-Tubulin

784

785

786

787

788

789

790

791

792

Bibliography

1. Cenini G, Hebisch M, Iefremova V, Flitsch LJ, Breitkreuz Y, Tanzi RE, Kim DY, Peitz M, Brustle O: **Dissecting Alzheimer's disease pathogenesis in human 2D and 3D models.** *Mol Cell Neurosci* 2021, **110:**103568.

2. Serrano-Pozo A, Frosch MP, Masliah E, Hyman BT: **Neuropathological alterations in Alzheimer disease.** *Cold Spring Harb Perspect Med* 2011, **1:**a006189.

3. Qiu C, Kivipelto M, von Strauss E: **Epidemiology of Alzheimer's disease: occurrence, determinants, and strategies toward intervention.** *Dialogues Clin Neurosci* 2009, **11:**111-128.

4. D'Avanzo C, Aronson J, Kim YH, Choi SH, Tanzi RE, Kim DY: **Alzheimer's in 3D culture: challenges and perspectives.** *Bioessays* 2015, **37:**1139-1148.

5. Miller JA, Horvath S, Geschwind DH: **Divergence of human and mouse brain transcriptome highlights Alzheimer disease pathways.** *Proc Natl Acad Sci U S A* 2010, **107:**12698-12703.

6. Zhang Y, Sloan SA, Clarke LE, Caneda C, Plaza CA, Blumenthal PD, Vogel H, Steinberg GK, Edwards MS, Li G, et al: **Purification and Characterization of Progenitor and Mature Human Astrocytes Reveals Transcriptional and Functional Differences with Mouse.** *Neuron* 2016, **89:**37-53.

7. Arranz AM, De Strooper B: **The role of astroglia in Alzheimer's disease: pathophysiology and clinical implications.** *Lancet Neurol* 2019, **18:**406-414.

814 8. Penney J, Ralvenius WT, Tsai LH: **Modeling Alzheimer's disease with iPSC-derived brain**
815 **cells.** *Mol Psychiatry* 2020, **25:**148-167.

816 9. Lagomarsino VN, Pearse RV, Liu L, Hsieh Y-C, Fernandez MA, Vinton EA, Paull D, Felsky D,
817 Tasaki S, Gaiteri C, et al: **Stem cell-derived neurons reflect features of protein networks,**
818 **neuropathology, and cognitive outcome of their aged human donors.** *Neuron* 2021,
819 **109:**3402-3420.e3409.

820 10. Cantley W, Du C, Lomoio S, DePalma T, Peirent E, Kleinknecht D, Hunter M, Tang-Schomer
821 M, Tesco G, Kaplan D: **Functional and Sustainable 3D Human Neural Network Models**
822 **from Pluripotent Stem Cells.** *ACS Biomater Sci Eng,* 2018, **Article ASAP DOI:**
823 **10.1021/acsbiomaterials.8b00622 Publication Date (Web): October 1, 2018**.

824 11. Tang-Schomer MD, White JD, Tien LW, Schmitt LI, Valentin TM, Graziano DJ, Hopkins AM,
825 Omenetto FG, Haydon PG, Kaplan DL: **Bioengineered functional brain-like cortical tissue.**
826 *Proceedings of the National Academy of Sciences of the United States of America* 2014,
827 **111:**13811-13816.

828 12. Cairns DM, Rouleau N, Parker RN, Walsh KG, Gehrke L, Kaplan DL: **A 3D human brain-like**
829 **tissue model of herpes-induced Alzheimer's disease.** *Sci Adv* 2020, **6:**eaay8828.

830 13. Cairns DM, Chwalek K, Moore YE, Kelley MR, Abbott RD, Moss S, Kaplan DL: **Expandable**
831 **and rapidly differentiating human induced neural stem cell lines for multiple tissue**
832 **engineering applications.** *Stem cell reports* 2016, **7:**557-570.

833 14. Rouleau N, Cantley WL, Liaudanskaya V, Berk A, Du C, Rusk W, Peirent E, Koester C,
834 Nieland TJF, Kaplan DL: **A Long-Living Bioengineered Neural Tissue Platform to Study**
835 **Neurodegeneration.** *Macromolecular Bioscience* 2020, **20:**e2000004.

836 15. Muratore CR, Rice HC, Srikanth P, Callahan DG, Shin T, Benjamin LN, Walsh DM, Selkoe
837 DJ, Young-Pearse TL: **The familial Alzheimer's disease APPV717I mutation alters APP**
838 **processing and Tau expression in iPSC-derived neurons.** *Hum Mol Genet* 2014, **23:**3523-
839 3536.

840 16. Hector A, Brouillette J: **Hyperactivity Induced by Soluble Amyloid-beta Oligomers in the**
841 **Early Stages of Alzheimer's Disease.** *Front Mol Neurosci* 2020, **13:**600084.

842 17. Wan YW, Al-Ouran R, Mangleburg CG, Perumal TM, Lee TV, Allison K, Swarup V, Funk CC,
843 Gaiteri C, Allen M, et al: **Meta-Analysis of the Alzheimer's Disease Human Brain**
844 **Transcriptome and Functional Dissection in Mouse Models.** *Cell Rep* 2020, **32:**107908.

845 18. Chwalek K, Tang-Schomer MD, Omenetto FG, Kaplan DL: **In vitro bioengineered model of**
846 **cortical brain tissue.** *Nature Protocols* 2015, **10:**1362-1373.

847 19. Nazarov R, Jin HJ, Kaplan DL: **Porous 3-D scaffolds from regenerated silk fibroin.**
848 *Biomacromolecules* 2004, **5:**718-726.

849 20. Muratore CR, Srikanth P, Callahan DG, Young-Pearse TL: **Comparison and optimization**
850 **of hiPSC forebrain cortical differentiation protocols.** *Plos One* 2014, **9:**e105807.

851 21. Itskovitz-Eldor J, Schuldiner M, Karsenti D, Eden A, Yanuka O, Amit M, Soreq H, Benvenisty
852 N: **Differentiation of human embryonic stem cells into embryoid bodies compromising**
853 **the three embryonic germ layers.** *Molecular Medicine* 2000, **6:**88-95.

854 22. Zeng H, Guo M, Martins-Taylor K, Wang X, Zhang Z, Park JW, Zhan S, Kronenberg MS,
855 Lichtler A, Liu H-X, et al: **Specification of region-specific neurons including forebrain**
856 **glutamatergic neurons from human induced pluripotent stem cells.** *Plos One* 2010,
857 **5:**e11853.

858 23. Muratore CR, Zhou C, Liao M, Fernandez MA, Taylor WM, Lagomarsino VN, Pearse RV, Rice
859 HC, Negri JM, He A, et al: **Cell-type Dependent Alzheimer's Disease Phenotypes: Probing**
860 **the Biology of Selective Neuronal Vulnerability.** *Stem cell reports* 2017, **9:**1868-1884.

861 24. Engle SJ, Blaha L, Kleiman RJ: **Best Practices for Translational Disease Modeling Using**
862 **Human iPSC-Derived Neurons.** *Neuron* 2018, **100:**783-797.

863 25. Pettinato G, Wen X, Zhang N: **Formation of well-defined embryoid bodies from**
864 **dissociated human induced pluripotent stem cells using microfabricated cell-repellent**
865 **microwell arrays.** *Sci Rep* 2014, **4:**7402.

866 26. Topol A, Tran NN, Brennand KJ: **A guide to generating and using hiPSC derived NPCs**
867 **for the study of neurological diseases.** *J Vis Exp* 2015**:**e52495.

868 27. Readhead B, Hartley BJ, Eastwood BJ, Collier DA, Evans D, Farias R, He C, Hoffman G,
869 Sklar P, Dudley JT, et al: **Expression-based drug screening of neural progenitor cells**
870 **from individuals with schizophrenia.** *Nat Commun* 2018, **9:**4412.

871 28. Bennett DA, Buchman AS, Boyle PA, Barnes LL, Wilson RS, Schneider JA: **Religious Orders**
872 **Study and Rush Memory and Aging Project.** *J Alzheimers Dis* 2018, **64:**S161-S189.

873 29. Danaher P, Warren S, Dennis L, D'Amico L, White A, Disis ML, Geller MA, Odunsi K,
874 Beechem J, Fling SP: **Gene expression markers of Tumor Infiltrating Leukocytes.** *J*
875 *Immunother Cancer* 2017, **5:**18.

876 30. Zhang Y, Pak C, Han Y, Ahlenius H, Zhang Z, Chanda S, Marro S, Patzke C, Acuna C, Covy
877 J, et al: **Rapid single-step induction of functional neurons from human pluripotent stem**
878 **cells.** *Neuron* 2013, **78:**785-798.

879 31. Nehme R, Zuccaro E, Ghosh SD, Li C, Sherwood JL, Pietilainen O, Barrett LE, Limone F,
880 Worringer KA, Kommineni S, et al: **Combining NGN2 Programming with Developmental**
881 **Patterning Generates Human Excitatory Neurons with NMDAR-Mediated Synaptic**
882 **Transmission.** *Cell reports* 2018, **23:**2509-2523.

883 32. Liao M-C, Muratore CR, Gierahn TM, Sullivan SE, Srikanth P, De Jager PL, Love JC, Young-
884 Pearse TL: **Single-Cell Detection of Secreted Aβ and sAPPα from Human IPSC-Derived**
885 **Neurons and Astrocytes.** *The Journal of Neuroscience* 2016, **36:**1730-1746.

886 33. Mariani J, Simonini MV, Palejev D, Tomasini L, Coppola G, Szekely AM, Horvath TL,
887 Vaccarino FM: **Modeling human cortical development in vitro using induced pluripotent**
888 **stem cells.** *Proc Natl Acad Sci U S A* 2012, **109:**12770-12775.

889 34. Arber C, Toombs J, Lovejoy C, Ryan NS, Paterson RW, Willumsen N, Gkanatsiou E, Portelius
890 E, Blennow K, Heslegrave A, et al: **Familial Alzheimer's disease patient-derived neurons**
891 **reveal distinct mutation-specific effects on amyloid beta.** *Mol Psychiatry* 2020, **25:**2919-
892 2931.

893 35. O'Connor A, Pannee J, Poole T, Arber C, Portelius E, Swift IJ, Heslegrave AJ, Abel E,
894 Willumsen N, Rice H, et al: **Plasma amyloid-beta ratios in autosomal dominant**
895 **Alzheimer's disease: the influence of genotype.** *Brain* 2021, **144:**2964-2970.

896 36. Eimer WA, Vassar R: **Neuron loss in the 5XFAD mouse model of Alzheimer's disease**
897 **correlates with intraneuronal Abeta42 accumulation and Caspase-3 activation.** *Mol*
898 *Neurodegener* 2013, **8:**2.

899 37. Du C, Collins W, Cantley W, Sood D, Kaplan DL: **Tutorials for Electrophysiological**
900 **Recordings in Neuronal Tissue Engineering.** *ACS Biomater Sci Eng* 2017, **3:**2235-2246.

901 38. Lam AD, Deck G, Goldman A, Eskandar EN, Noebels J, Cole AJ: **Silent hippocampal**
902 **seizures and spikes identified by foramen ovale electrodes in Alzheimer's disease.** *Nat*
903 *Med* 2017, **23:**678-680.

904 39. Vossel KA, Beagle AJ, Rabinovici GD, Shu H, Lee SE, Naasan G, Hegde M, Cornes SB,
905 Henry ML, Nelson AB, et al: **Seizures and epileptiform activity in the early stages of**
906 **Alzheimer disease.** *JAMA neurology* 2013, **70:**1158-1166.

907 40. Zott B, Busche MA, Sperling RA, Konnerth A: **What Happens with the Circuit in Alzheimer's**
908 **Disease in Mice and Humans?** *Annu Rev Neurosci* 2018, **41:**277-297.

909 41. Zott B, Simon MM, Hong W, Unger F, Chen-Engerer HJ, Frosch MP, Sakmann B, Walsh DM,
910 Konnerth A: **A vicious cycle of beta amyloid-dependent neuronal hyperactivation.**
911 *Science* 2019, **365:**559-565.

912 42. Palop JJ, Chin J, Roberson ED, Wang J, Thwin MT, Bien-Ly N, Yoo J, Ho KO, Yu G-Q,
913 Kreitzer A, et al: **Aberrant excitatory neuronal activity and compensatory remodeling of**
914 **inhibitory hippocampal circuits in mouse models of Alzheimer's disease.** *Neuron* 2007,
915 **55:**697-711.

916 43. Palop JJ, Mucke L: **Network abnormalities and interneuron dysfunction in Alzheimer**
917 **disease.** *Nature Reviews Neuroscience* 2016, **17:**777-792.

918 44. Palop JJ, Mucke L: **Amyloid-beta-induced neuronal dysfunction in Alzheimer's disease:**
919 **from synapses toward neural networks.** *Nature Neuroscience* 2010, **13:**812-818.

920 45. Palop JJ, Mucke L: **Epilepsy and cognitive impairments in Alzheimer disease.** *Arch*
921 *Neurol* 2009, **66:**435-440.

922 46. Busche MA, Chen X, Henning HA, Reichwald J, Staufenbiel M, Sakmann B, Konnerth A:
923 **Critical role of soluble amyloid-beta for early hippocampal hyperactivity in a mouse**
924 **model of Alzheimer's disease.** *Proc Natl Acad Sci U S A* 2012, **109:**8740-8745.

925 47. Busche MA, Eichhoff G, Adelsberger H, Abramowski D, Wiederhold K-H, Haass C,
926 Staufenbiel M, Konnerth A, Garaschuk O: **Clusters of hyperactive neurons near amyloid**
927 **plaques in a mouse model of Alzheimer's disease.** *Science* 2008, **321:**1686-1689.

928 48. Busche MA, Grienberger C, Keskin AD, Song B, Neumann U, Staufenbiel M, Forstl H,
929 Konnerth A: **Decreased amyloid-beta and increased neuronal hyperactivity by**
930 **immunotherapy in Alzheimer's models.** *Nat Neurosci* 2015, **18:**1725-1727.

931 49. Ormel PR, Vieira de Sa R, van Bodegraven EJ, Karst H, Harschnitz O, Sneeboer MAM,
932 Johansen LE, van Dijk RE, Scheefhals N, Berdenis van Berlekom A, et al: **Microglia innately**
933 **develop within cerebral organoids.** *Nat Commun* 2018, **9:**4167.

934 50. Quadrato G, Nguyen T, Macosko EZ, Sherwood JL, Min Yang S, Berger DR, Maria N,
935 Scholvin J, Goldman M, Kinney JP, et al: **Cell diversity and network dynamics in**
936 **photosensitive human brain organoids.** *Nature* 2017, **545:**48-53.

937 51. Preuss C, Pandey R, Piazza E, Fine A, Uyar A, Perumal T, Garceau D, Kotredes KP, Williams
938 H, Mangravite LM, et al: **A novel systems biology approach to evaluate mouse models**
939 **of late-onset Alzheimer's disease.** *Mol Neurodegener* 2020, **15:**67.

940 52. Bateman RJ, Xiong C, Benzinger TL, Fagan AM, Goate A, Fox NC, Marcus DS, Cairns NJ,
941 Xie X, Blazey TM, et al: **Clinical and biomarker changes in dominantly inherited**
942 **Alzheimer's disease.** *N Engl J Med* 2012, **367:**795-804.

943 53. Mondadori CR, Buchmann A, Mustovic H, Schmidt CF, Boesiger P, Nitsch RM, Hock C,
944 Streffer J, Henke K: **Enhanced brain activity may precede the diagnosis of Alzheimer's**
945 **disease by 30 years.** *Brain* 2006, **129:**2908-2922.

946 54. Reiman EM, Quiroz YT, Fleisher AS, Chen K, Velez-Pardo C, Jimenez-Del-Rio M, Fagan AM,
947 Shah AR, Alvarez S, Arbelaez A, et al: **Brain imaging and fluid biomarker analysis in**
948 **young adults at genetic risk for autosomal dominant Alzheimer's disease in the**
949 **presenilin 1 E280A kindred: a case-control study.** *Lancet Neurol* 2012, **11:**1048-1056.

950 55. Ghatak S, Dolatabadi N, Trudler D, Zhang X, Wu Y, Mohata M, Ambasudhan R, Talantova M,
951 Lipton SA: **Mechanisms of hyperexcitability in Alzheimer's disease hiPSC-derived**
952 **neurons and cerebral organoids vs isogenic controls.** *Elife* 2019, **8**.

953 56. Allen M, Carrasquillo MM, Funk C, Heavner BD, Zou F, Younkin CS, Burgess JD, Chai HS,
954 Crook J, Eddy JA, et al: **Human whole genome genotype and transcriptome data for**
955 **Alzheimer's and other neurodegenerative diseases.** *Sci Data* 2016, **3:**160089.

956 57. De Jager PL, Ma Y, McCabe C, Xu J, Vardarajan BN, Felsky D, Klein HU, White CC, Peters
957 MA, Lodgson B, et al: **A multi-omic atlas of the human frontal cortex for aging and**
958 **Alzheimer's disease research.** *Sci Data* 2018, **5:**180142.

959 58. Wang M, Beckmann ND, Roussos P, Wang E, Zhou X, Wang Q, Ming C, Neff R, Ma W,
960 Fullard JF, et al: **The Mount Sinai cohort of large-scale genomic, transcriptomic and**
961 **proteomic data in Alzheimer's disease.** *Sci Data* 2018, **5:**180185.

962 59. Mertens J, Reid D, Lau S, Kim Y, Gage FH: **Aging in a Dish: iPSC-Derived and Directly**
963 **Induced Neurons for Studying Brain Aging and Age-Related Neurodegenerative**
964 **Diseases.** *Annu Rev Genet* 2018, **52:**271-293.

965 60. Golde TE: **Alzheimer's disease - the journey of a healthy brain into organ failure.** *Mol*
966 *Neurodegener* 2022, **17:**18.

967 61. Hronik-Tupaj M, Raja WK, Tang-Schomer M, Omenetto FG, Kaplan DL: **Neural responses**
968 **to electrical stimulation on patterned silk films.** *J Biomed Mater Res A* 2013, **101:**2559-
969 2572.

970 62. Tang-Schomer MD, Hu X, Tupaj M, Tien LW, Whalen M, Omenetto F, Kaplan DL: **Film-based**
971 **Implants for Supporting Neuron-Electrode Integrated Interfaces for The Brain.** *Adv*
972 *Funct Mater* 2014, **24:**1938-1948.

973 63. Ramos DM, Skarnes WC, Singleton AB, Cookson MR, Ward ME: **Tackling**
974 **neurodegenerative diseases with genomic engineering: A new stem cell initiative from**
975 **the NIH.** *Neuron* 2021, **109:**1080-1083.

976 64. Rockwood DN, Preda RC, Yucel T, Wang X, Lovett ML, Kaplan DL: **Materials fabrication**
977 **from Bombyx mori silk fibroin.** *Nat Protoc* 2011, **6:**1612-1631.

978 65. Perkins JR, Dawes JM, McMahon SB, Bennett DL, Orengo C, Kohl M: **ReadqPCR and**
979 **NormqPCR: R packages for the reading, quality checking and normalisation of RT-**
980 **qPCR quantification cycle (Cq) data.** *BMC Genomics* 2012, **13:**296.

981 66. Ferreira JA: **The Benjamini-Hochberg method in the case of discrete test statistics.** *Int J*
982 *Biostat* 2007, **3:**Article 11.

983 67. Mostafavi S, Gaiteri C, Sullivan SE, White CC, Tasaki S, Xu J, Taga M, Klein HU, Patrick E,
984 Komashko V, et al: **A molecular network of the aging human brain provides insights into**
985 **the pathology and cognitive decline of Alzheimer's disease.** *Nat Neurosci* 2018, **21:**811-
986 819.

987 68. Pandey RS, Graham L, Uyar A, Preuss C, Howell GR, Carter GW: **Genetic perturbations of**
988 **disease risk genes in mice capture transcriptomic signatures of late-onset Alzheimer's**
989 **disease.** *Mol Neurodegener* 2019, **14:**50.

990

991

992

993

994

995

996

997

998

999

1000

1001

1002

1003 **Figures**

1004 **Figure 1**

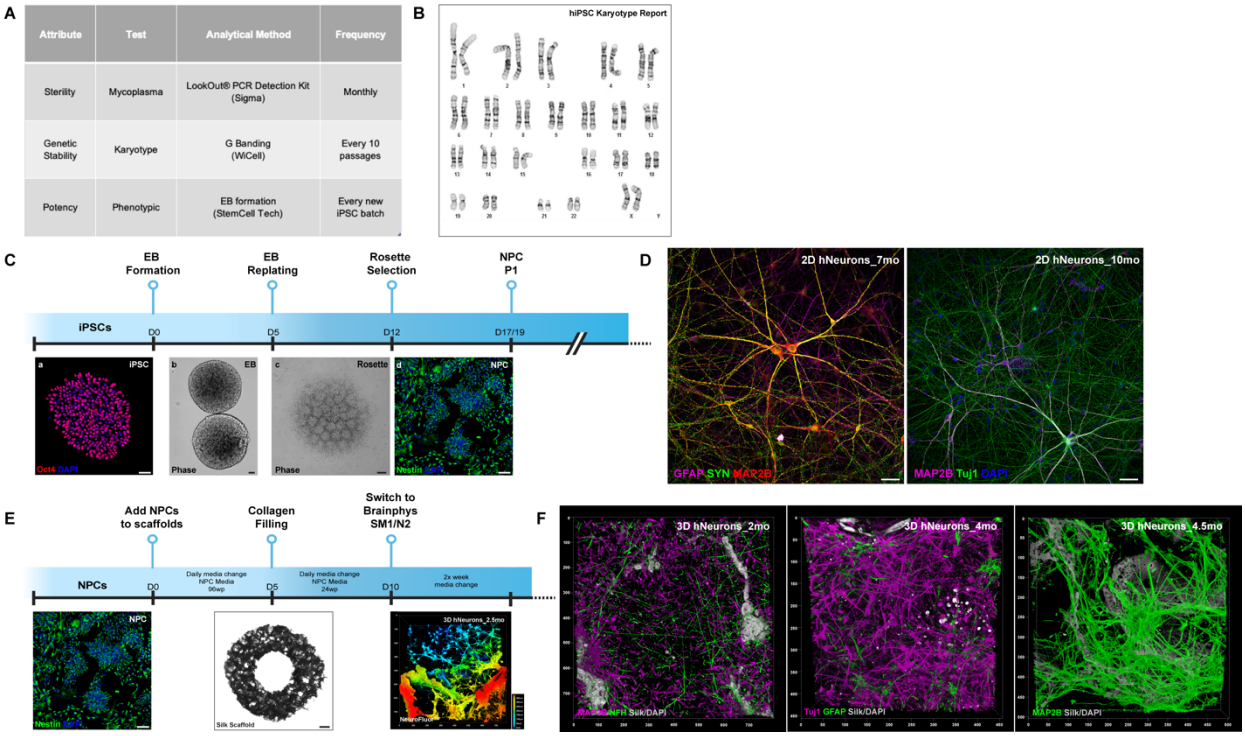

1005

1006

1007 **Figure 1. A 3D bioengineered silk-collagen neural model**. (A) Quality tests performed on
1008 iPSCs used in this study. (B) Representative karyotype report. Reports for all the lines are in Fig.
1009 S1. (C) Schematic representation of the differentiation timeline to generate NPCs. (a)
1010 Representative iPSC colony stained for Oct4 (red) and DAPI (blue). Scale bar: 40um. Confocal
1011 z-stack. Leica SP8 HC PL APO CS2 20x/0.75 IMM. 1.5x Zoom. EB (b) and rosettes (c) phase-
1012 contrast images. Scale bar: 20um. Nikon TE300 CFI PL FL DL 4x/0.13 and 10x/0.30. (d) NPC
1013 cultures stained for nestin (green) and DAPI (blue). Scale bar: 40um. Confocal z-stack. Leica SP8
1014 HC PL APO CS2 20x/0.75 IMM. 1x Zoom. (D) 2D 7-months-old hNeurons stained for GFAP
1015 (magenta), SYN (green), and MAP2B (red), and 10-months-old hNeurons stained for MAP2B
1016 (magenta), Tuj1 (green), and DAPI (blue). Scale bar: 50um. Confocal z-stack. Leica SP8 HC PL
1017 APO CS2 20x/0.75 IMM. 0.75x Zoom. (E) Schematic representation of the timeline to differentiate

1018 hNeurons in silk-collagen scaffolds from NPCs. Silk scaffold phase-contrast image. Scale bar:
1019 500um. Z-stack. Stitched image. Zeiss CD7 PL APO 5x/0.35. Magnification changer 0.5x. 3D
1020 reconstruction of hNeurons grown in a scaffold for 2.5 months and stained with NeuroFluor™
1021 NeuO. Leica SP8 HC PL APO CS2 20x/0.75 IMM. 0.75x Zoom. (F) 3D reconstruction of hNeurons
1022 grown in a scaffold for 2 months (stained for MAP2B (magenta), NFH (green)), 4 months (stained
1023 for Tuj1 (magenta), GFAP (green)) and 4.5 months (stained for MAP2B (green)). For all the
1024 images DAPI and silk autofluorescent signals are in grey. Leica SP8 HC PL APO CS2 20x/0.75
1025 IMM. 0.75x Zoom.

1026

1027

1028

1029

1030

1031

1032

1033

1034

1035

1036

1037 **Figure 2**

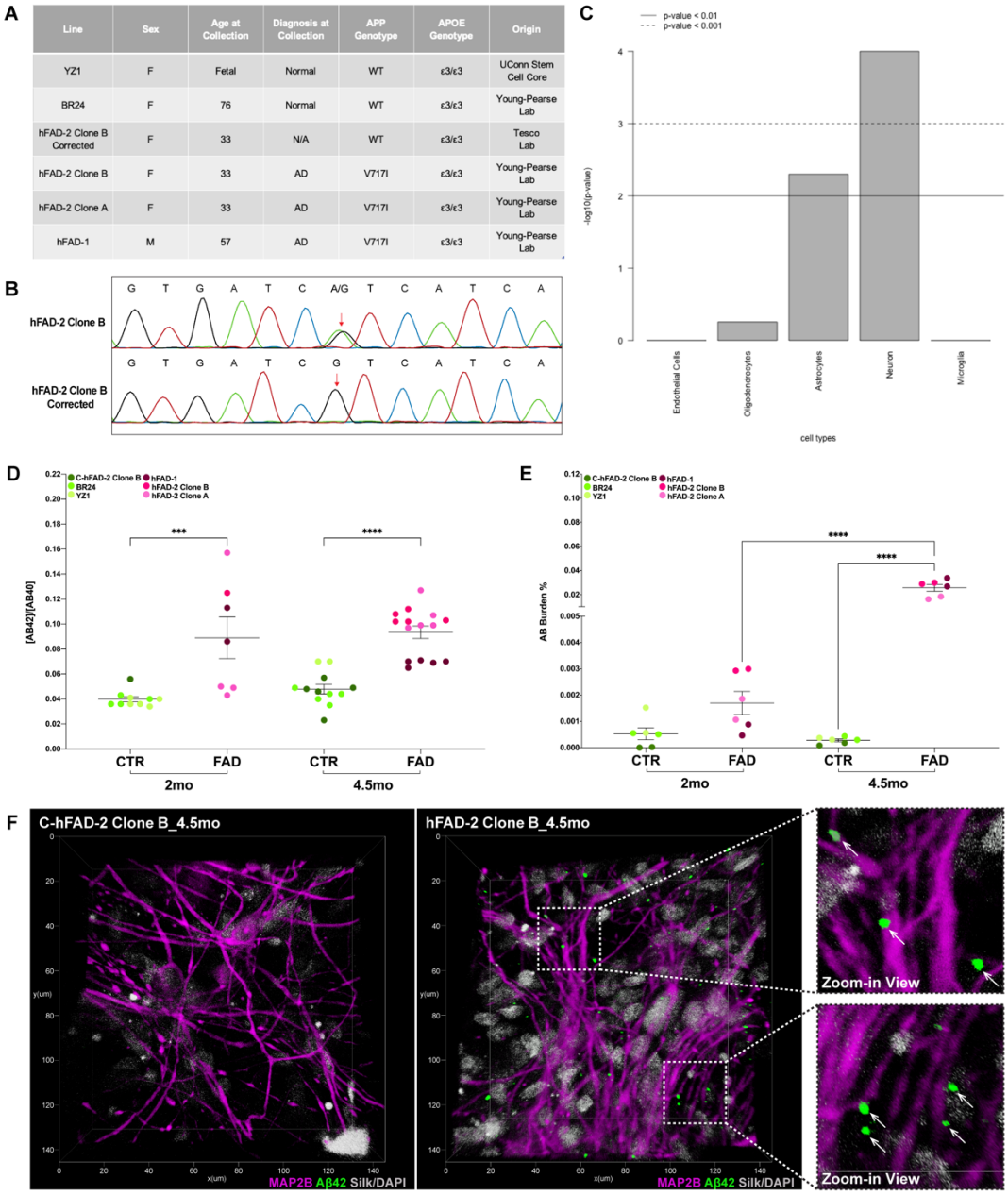

1038

1039 **Figure 2. Aβ42/40 ratio and extracellular Aβ42 deposition are elevated in FAD cultures.** (A)

1040 Table reporting iPS lines used across the study. (B) Sequencing traces of hFAD-2 Clone B and

1041 its isogenic control after reversion of the APP V717I mutation (C-hFAD-2 Clone B). (C) nSolver

1042 Cell Enrichment analysis bar plot. (D) Aβ42/40 MSD analysis quantification in conditioned media.

1043 FAD cultures (hFAD-1, hFAD-2 Clone A, hFAD-2 Clone B) and controls (C-hFAD-2 Clone B,
1044 BR24, YZ1) plotted as groups are provided at 2 and 4.5 months. CTR 2mo: n=10, FAD 2mo: n=7,
1045 CTR 4.5mo: n=12, FAD 4.5mo: n=15. One-way ANOVA, Tukey's post-hoc test. (E) Amyloid
1046 burden quantification (%). FAD cultures (hFAD-1, hFAD-2 Clone A, hFAD-2 Clone B) and controls
1047 (C-hFAD-2 Clone B, BR24, YZ1) plotted as groups are provided at 2 and 4.5 months. n=6. One-
1048 way ANOVA, Tukey's post-hoc test. (E) Representative 3D reconstructions of hNeuron culture
1049 (4.5 months) derived from C-hFAD-2 Clone B and hFAD-2 Clone B stained for MAP2B (magenta)
1050 and Aβ42 (green). DAPI and silk autofluorescent signals are in grey. Zoom-in view: green Aβ42
1051 extracellular depositions (white arrows) interspersed among hNeurons (MAP2B, magenta). Leica
1052 Falcon SP8 HC PL APO CS2 20x/0.75 IMM. 3.5x Zoom.

1053 **Figure 3**

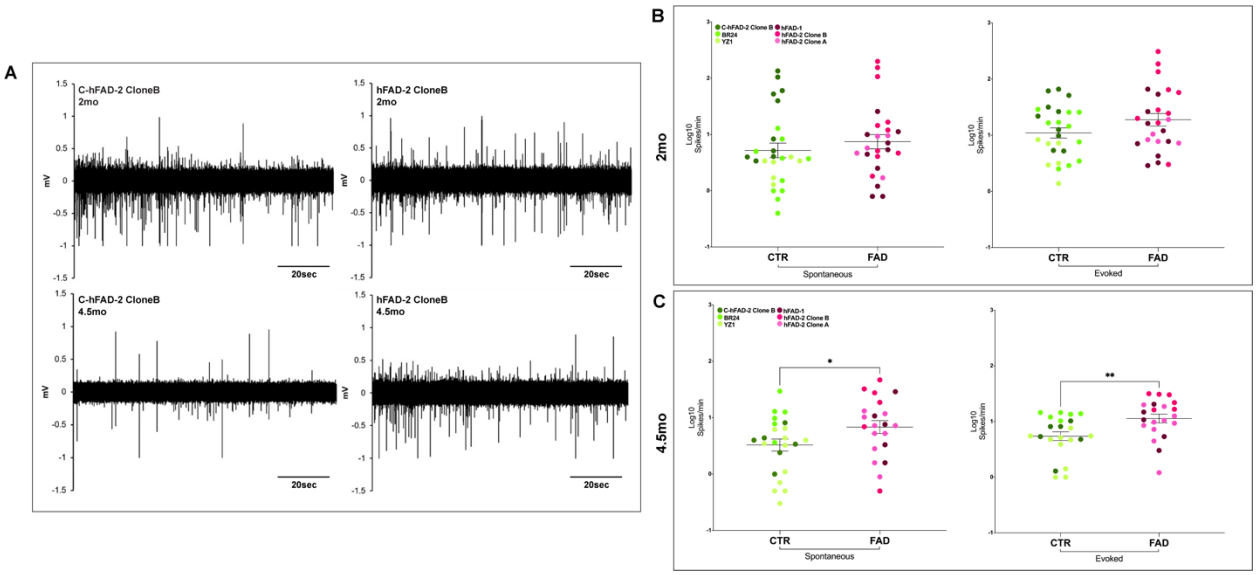

1054

1055 **Figure 3. FAD cultures manifest enhanced neuronal excitability.** (A) Representative traces
1056 of spontaneous LFPs (mV) obtained from 3D cultures derived from a FAD line (hFAD-2 Clone B)
1057 and the isogenic control (C-hFAD-2 Clone B) at 2 months and 4.5 months. A 20-sec reference is
1058 provided for traces. Quantification of normalized spontaneous and evoked LFP spikes/min

1059 (Log10) at 2 months (B) and 4.5 months (C). FAD cultures (hFAD-1, hFAD-2 Clone A, hFAD-2
1060 Clone B) and controls (C-hFAD-2 Clone B, BR24, YZ1) plotted as groups are provided. (B)
1061 Spontaneous CTR 2mo n=26, FAD 2mo n=25. Evoked CTR 2mo n=26, FAD 2mo n=25. (C)
1062 Spontaneous CTR 4.5mo n=23, FAD 4.5mo n=21. Evoked CTR 4.5mo n=22, FAD 4.5mo n=21.
1063 Unpaired t-test.

1064 **Figure 4**

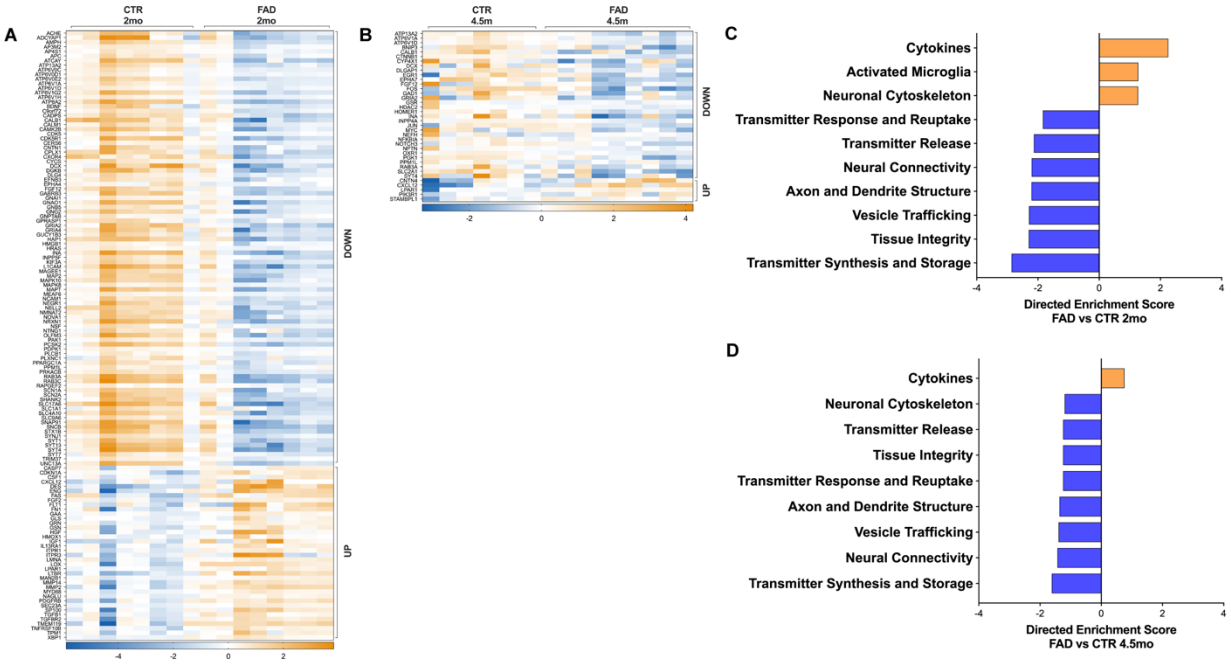

1065

1066 **Figure 4**. **Differential expression and functional analysis of the NanoString panel in FAD**
1067 **cultures**. DEGs (absolute fold change > 1.5, FDR < 0.05) in 2-months-old (A) and 4.5-months-
1068 old (B) CTR and FAD lines, are shown in the heatmap. GSA of differentially expressed genes in
1069 iPSC-derived cultures (FAD vs CTR, ROSALIND® platform, NanoString annotations) at 2 months
1070 (C) and 4.5 months (D). Upregulation: directed enrichment score > 0. Downregulation: directed
1071 enrichment score < 0. FAD 2mo n=8, CTR 2mo n=8, FAD 4.5mo n=9, CTR 4.5mo n=7.

1072

1073 **Figure 5**

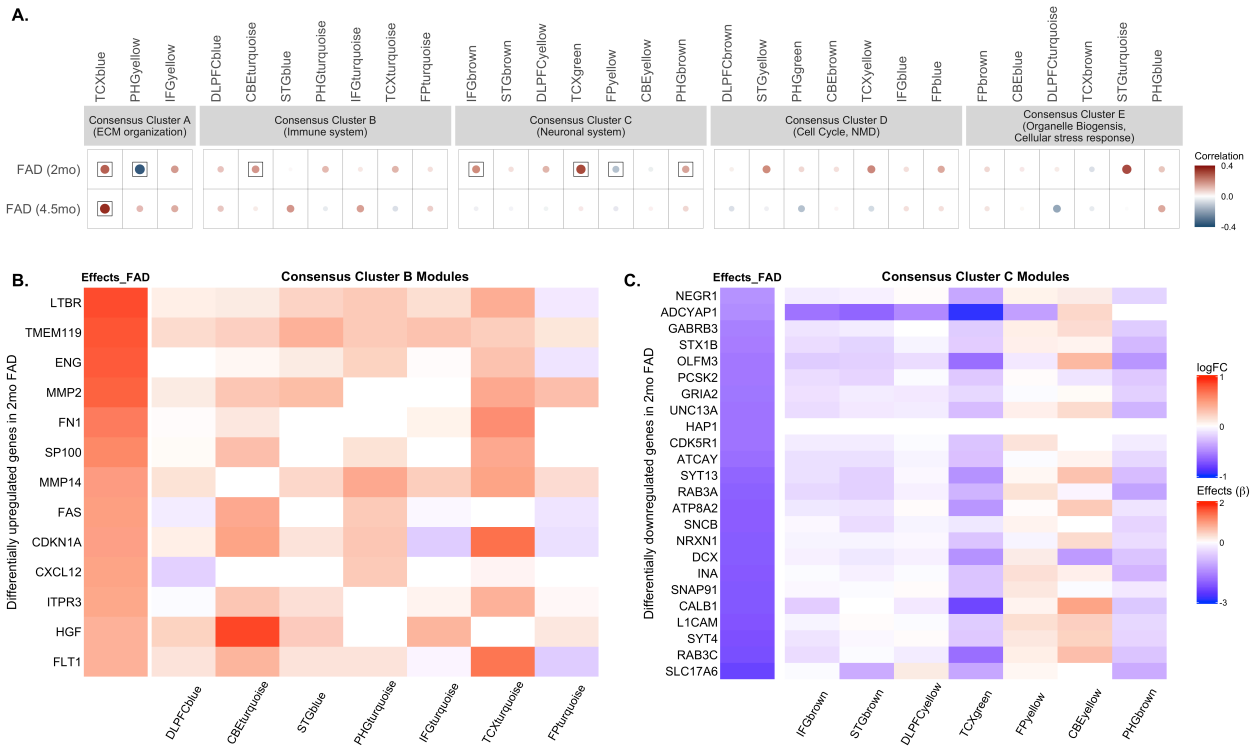

1074

1075 **Figure 5. FAD cultures reproduce human neurodegeneration signatures.** Correlation
1076 analysis between the gene expression profile of FAD cultures and human post-mortem co-
1077 expression modules. (A) 2-months-old FAD cultures exhibited a significant positive correlation (p
1078 < 0.05) with AD changes in immune-related modules in Consensus Cluster B and neuronal related
1079 modules in Consensus Cluster C. Circles within a square correspond to significant ($p < 0.05$)
1080 positive (red) and negative (blue) Pearson correlation coefficients for gene expression changes
1081 in FAD lines associated with disease-associated changes in distinct human co-expression
1082 modules. Color intensity and size of the circles are proportional to the correlation. (B) Differentially
1083 upregulated genes in the 2 months old FAD lines (FDR <0.05, fold change > 1.5), showing
1084 increased expression in immune/inflammation associated AMP-AD modules in Consensus
1085 Cluster B, are shown in the heatmap. (C) Differentially downregulated genes in the 2 months old

FAD lines (FDR <0.05, fold change < 1.5), exhibiting reduced expression in neuronal-associated AMP-AD modules in Consensus Cluster C, are shown in the heatmap. FAD 2mo n=8, CTR 2mo n=8.

Figure S1

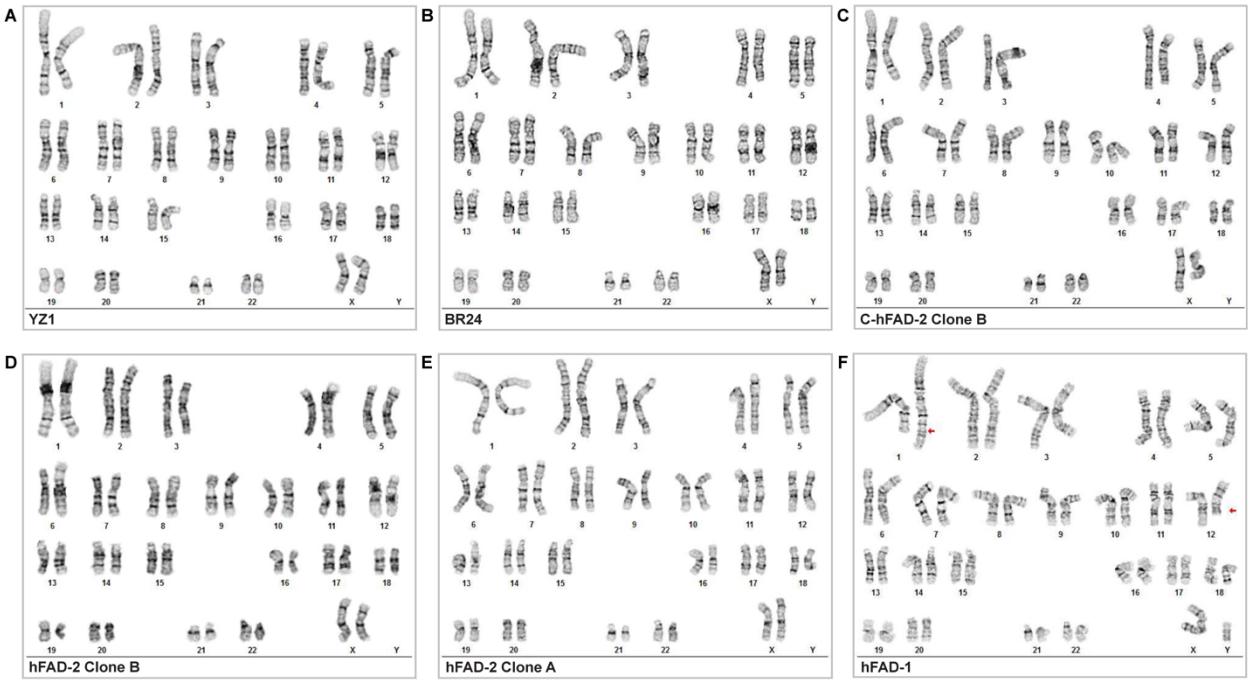

Figure S1: Karyotype reports for all the lines used across the study (WiCell).

1097 **Figure S2**

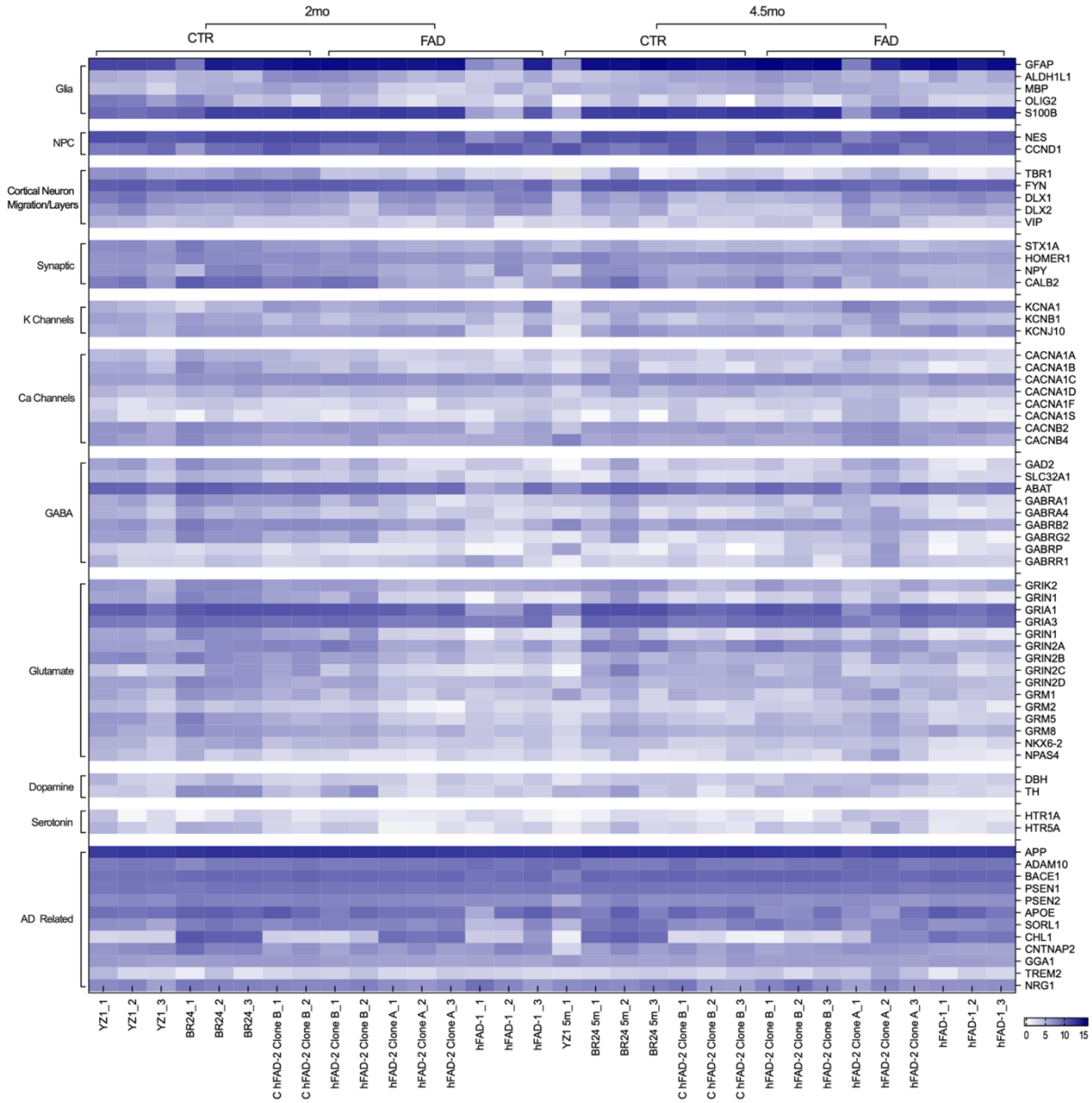

1098

1099 **Figure S2:** Normalized expression heatmap (9 housekeeping probes) of genes used to
1100 characterize the 3D cultures. FAD 2mo n=8, CTR 2mo n=8, FAD 4.5mo n=9, CTR 4.5mo n=7.
1101 Genes included in the heatmap are not deregulated when comparing FAD vs. CTR lines at any
1102 time point analyzed.

Figure S3

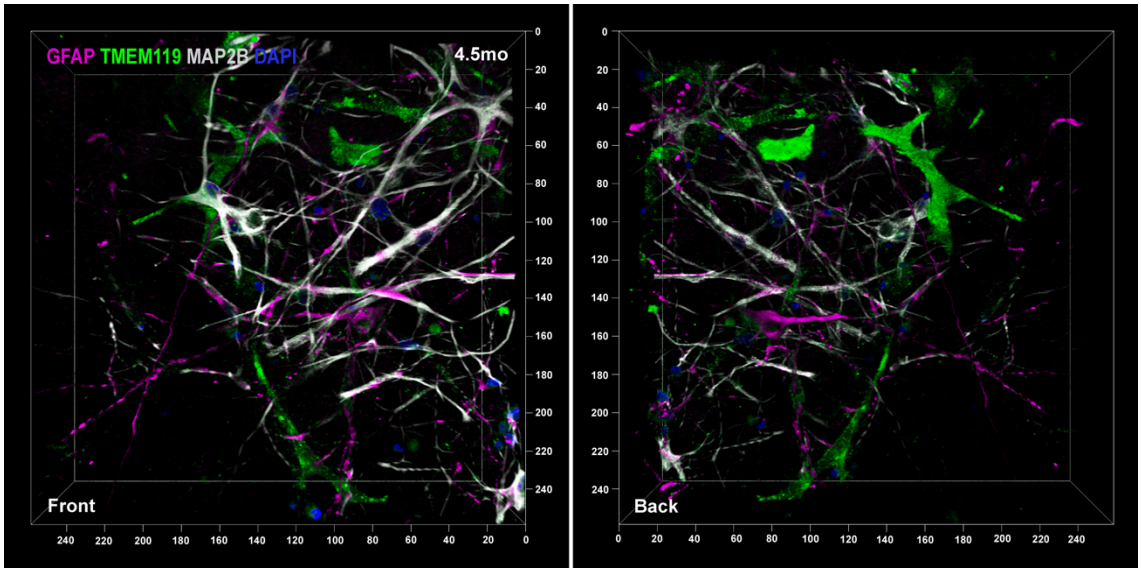

Figure S3: 3D reconstruction of 4.5 months cultures (stained for MAP2B (grey), TMEM119 (green), GFAP (magenta), DAPI (blue)). Front and back projections are shown. Leica Falcon SP8 HC PL APO CS2 20x/0.75 IMM. 2.25x Zoom.

Figure S4

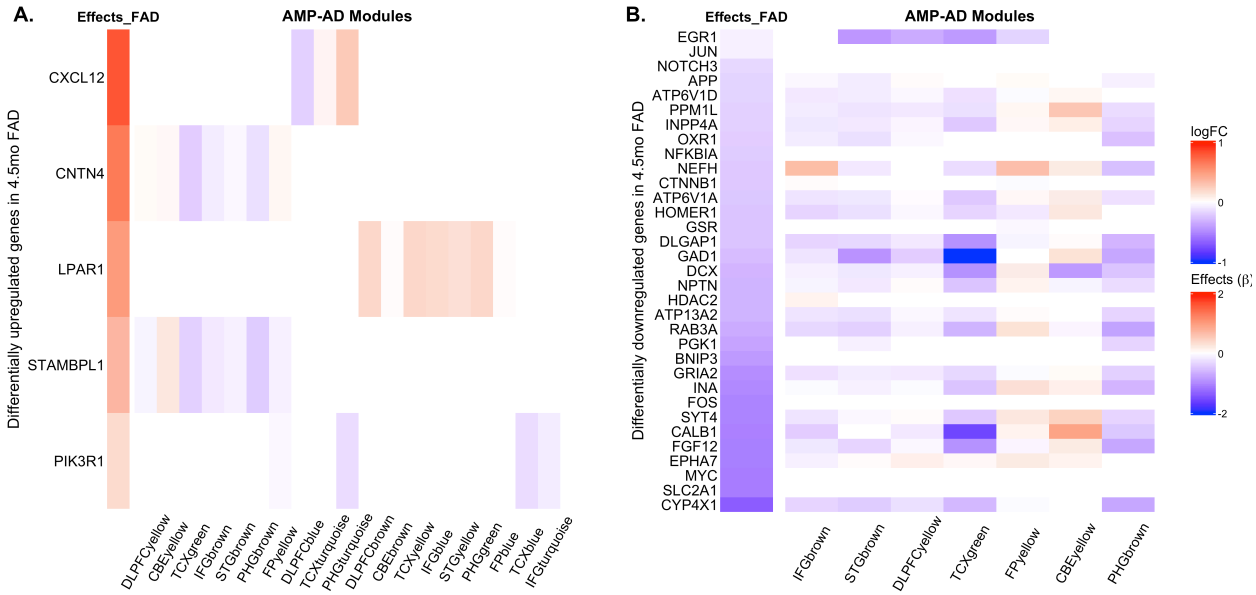

1110 **Figure S4:** Gene expression changes of differentially expressed genes in the 4.5-months-old
1111 FAD cultures across human co-expression modules. (A) Gene expression changes of five
1112 differentially upregulated genes in the 4.5-months-old FAD lines (FDR <0.05, fold change > 1.5)
1113 across AMP-AD modules are shown in the heatmap. (B) Gene expression changes of
1114 differentially downregulated genes in the 4.5-months-old FAD lines (FDR <0.05, fold change <
1115 1.5) across AMP-AD. FAD 4.5mo n=9, CTR 4.5mo n=7.

1116 **Table 1**

Target Antigen	Host	Clone	Clonality	Reactive Species	Company	Catalog #	IF Dilution	
							2D	3D
Aβ42	Rabbit	H31L21	Monoclonal	Human, Mouse	Invitrogen	700254	/	1:200
GFAP	Rabbit	/	Polyclonal	Human 90-95% homology between species	Dako	Z0334	1:1000	1:500
GFAP	Mouse	G-A-5	Monoclonal	Pig, Rat, Human	Sigma	G3893	/	1:500
MAP2B	Mouse	18	Monoclonal	Rat, Human, Mouse	BD Biosciences	610460	1:1000	1:500
MAP2B	Chicken	/	Polyclonal	Human, Rat, Bovine	Millipore	AB5543	1:1000	1:500
Nestin	Mouse	10C2	Monoclonal	Human Non-Human Primate	StemCell Tech	10C2	1:1000	/
NFH	Chicken	/	Polyclonal	Human, Rat, Mouse, Bovine, Porcine, Feline	Millipore	AB5539	/	1:500
OCT4	Mouse	3A2A20	Monoclonal	Human	StemCell Tech	60093	1:250	/
Synaptophysin 1	Mouse	7.2	Monoclonal	Human, Rat, Mouse, Mammals	Synaptic Systems	101011	1:500	/
TMEM119	Rabbit	/	Polyclonal	Human	Sigma	HPA051870	/	1:200
Tuj1	Mouse	TU-20	Monoclonal	Bovine, Rat, Avian, Monkey, Sheep, Human, Mouse, Pig	Chemicon	MAB1637	1:1000	1:500

1117

1118 **Table 1:** List of antibodies used throughout the study.

1119